



**HAL**  
open science

# Block Tectonics Across Western Tibet and Multi-Millennial Recurrence of Great Earthquakes on the Karakax Fault

H. Li, M. Chevalier, P. Tapponnier, J. Pan, Jerome van Der Woerd, A.  
Mériaux, F. Ryerson, G. Peltzer, Z. Sun, J. Si, et al.

► **To cite this version:**

H. Li, M. Chevalier, P. Tapponnier, J. Pan, Jerome van Der Woerd, et al.. Block Tectonics Across Western Tibet and Multi-Millennial Recurrence of Great Earthquakes on the Karakax Fault. *Journal of Geophysical Research: Solid Earth*, 2021, 126 (12), pp.e2021JB022033. 10.1029/2021JB022033 . hal-03517823

**HAL Id: hal-03517823**

**<https://hal.science/hal-03517823>**

Submitted on 12 Jan 2022

**HAL** is a multi-disciplinary open access archive for the deposit and dissemination of scientific research documents, whether they are published or not. The documents may come from teaching and research institutions in France or abroad, or from public or private research centers.

L'archive ouverte pluridisciplinaire **HAL**, est destinée au dépôt et à la diffusion de documents scientifiques de niveau recherche, publiés ou non, émanant des établissements d'enseignement et de recherche français ou étrangers, des laboratoires publics ou privés.



- 26       • Block tectonics and triple junction kinematics account for 24 Ma deformation of west  
27           Tibet and rise of  $\geq 8000$  m-high Karakorum range

28

29 **Abstract**

30           Fault slip rates are critical to quantify continental deformation. Those along the Karakax  
31 fault (northwestern Altyn Tagh Fault: ATF) have been debated, even though it is one of Tibet's  
32 most outstanding active faults. At Taersa, using LiDAR measurements of terrace and fan riser  
33 offsets (~6 to ~500 m) and  $^{10}\text{Be}/^{26}\text{Al}$  dating of alluvial surfaces (<210 ka), we obtain a late  
34 Quaternary slip rate of  $\sim 2.5 \pm 0.5$  mm/yr. This doubles the  $\sim 2.6 \pm 0.5$  mm/yr rate time span found  
35 to the east and west. We interpret the ~150 km-long, free-faced rupture along the fault to be that  
36 of the  $M \sim 7.6$  event felt in Hotan in 1882. Characteristic slip (~6 m) during four large  
37 earthquakes since ~10 ka implies a  $\sim 2500 \pm 500$  yrs return time. A ~3 mm/yr rate is consistent  
38 with the ~80 km offset of the Karakax river since uplift of the West Kunlun range and sediment  
39 deposition in the Tarim foreland accelerated, ~24 Ma ago. The faster slip rate (~10.5 mm/yr) on  
40 the central ATF matches the sum of those along the reactivated West Tibetan terrane boundaries  
41 (Karakax and Longmu-Gozha Co faults) at the Uzatagh triple junction (~36°N,  
42 83°E). The abrupt termination and altitude drop of the Karakorum range where the Longmu Co  
43 and Karakorum faults meet (Angmong junction), also reflect triple junction kinematics. Such  
44 localized changes account for the rise of the Karakorum and West Kunlun ranges and support  
45 lithospheric block tectonics rather than diffusely distributed deformation.

46

47 **Plain Language Summary**

48           How the Tibetan plateau rose to ~4500 m and deforms today remain outstanding  
49 questions. Tibet's northern edge follows the ~2000 km-long Altyn Tagh fault, whose  
50 westernmost branch is the Karakax fault. Despite the spectacular escarpments and offsets

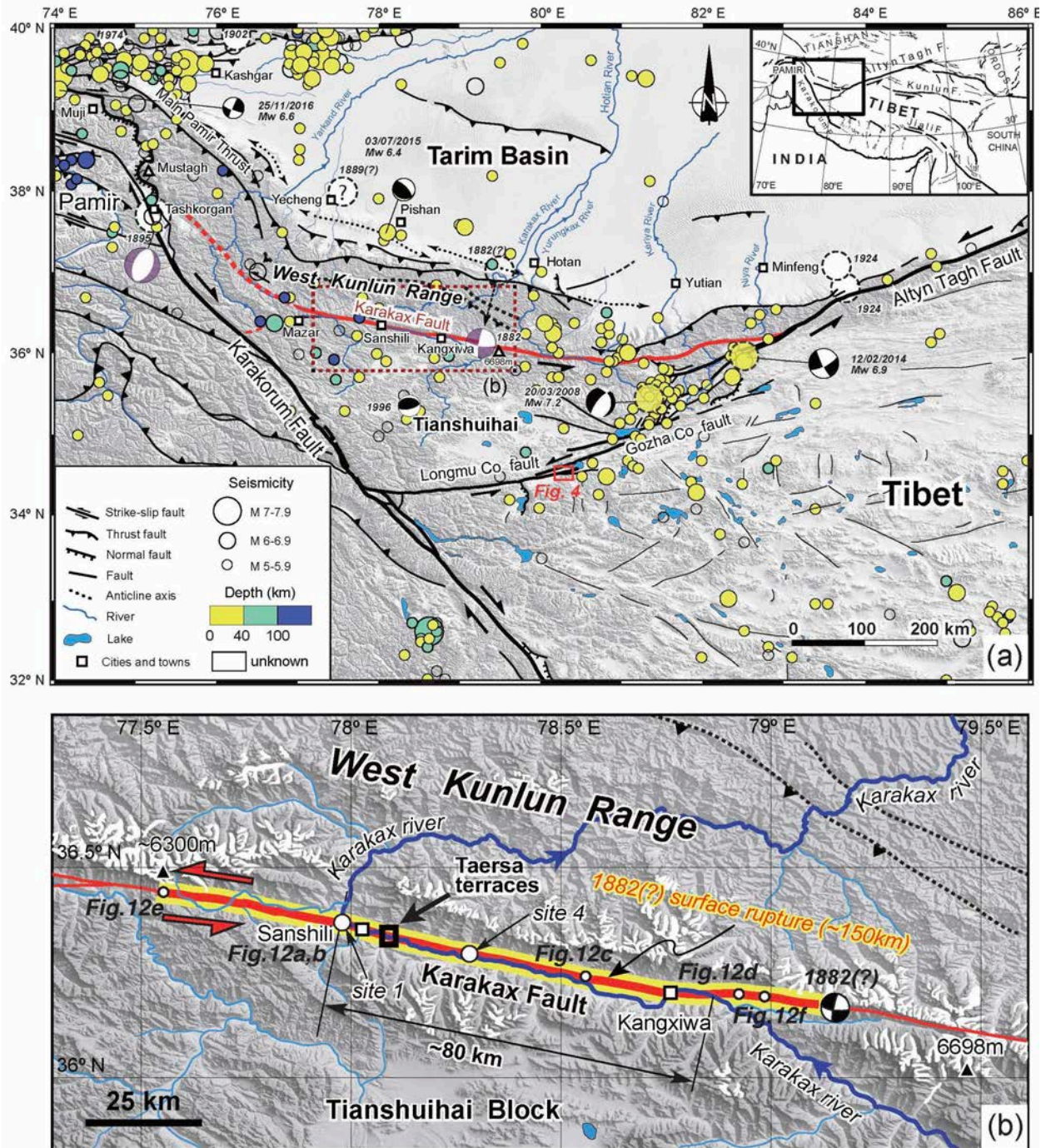
51 observed along that fault, its slip rate, critical to quantify continental deformation, has remained  
52 controversial. Here, we corroborate that, for the last ~210,000 yrs, that rate has been  $\sim 2.5 \pm 0.5$   
53 mm/yr, based on high-resolution topography and dating of left-laterally offset fluvial surfaces.  
54 The ~80 km offset of the Karakax river implies that this rate may have remained constant since  
55 the rise of the Kunlun range above the Tarim basin started ~24 Ma ago. The sharp fault trace  
56 reflects the exceptional preservation, since ~10,000 years ago, of four  $M \sim 7.6$  earthquake ruptures  
57 (the last in 1882), each with ~6 m of slip (~2500 yrs return time). Fault slip rates, GPS vectors  
58 and mountain altitudes across western Tibet reflect block motions and triple junction kinematics  
59 rather than continuum deformation. Specifically, localized velocity changes appear to account  
60 for the rise of the West Kunlun and Karakorum ranges. Our results bridge the gaps between  
61 present and long-term geological history, and broad-scale geodesy and local field evidence.

62

## 63 **1 Introduction**

64 The accurate determination of fault slip rates at various timescales is key to quantifying  
65 continental deformation kinematics, long-term seismicity and lithospheric rheology. Yet, because  
66 fault offsets and marker ages derived from different measurements and dating techniques are  
67 often difficult to constrain beyond doubt or to interpret jointly, and because slip-rates can be  
68 time-dependent (e.g., Chevalier et al., 2005), conflicting long-term slip rate values have been  
69 proposed along even the best studied active faults. In western Tibet, the longest segment of the  
70 ~400 km-long, ~100°E-striking Karakax fault (KXF), northwestern branch of the ~2000 km-long,  
71 left-lateral Altyn Tagh fault (ATF), is partly confined along the ~3-4 km-wide Karakax river  
72 valley. It follows the southern edge of the West Kunlun range, along the northern boundary of  
73 the Tianshuihai terrane (Fig. 1). Together with the sinistral Longmu-Gozha Co and dextral

74 Karakorum faults farther south, it contributes to absorb the convergence between India and Asia,  
75 and to steer the eastward extrusion of Tibet (e.g., Tapponnier and Molnar, 1977; Armijo et al.,  
76 1989; Avouac and Tapponnier, 1993; Tapponnier et al., 2001; Chevalier et al., 2017). Due to  
77 access restrictions and a remote location at ~3700 m, the KXF has been the target of few field  
78 studies (e.g., Matte et al., 1996; Li et al., 2012; Gong et al., 2017; Peltzer et al., 2020), in spite of  
79 spectacular, long-identified geomorphic markers (pull-apart basins, pressure ridges, and offset  
80 streams, terraces, fans and moraines) (Peltzer et al., 1989).



81  
 82 **Figure 1.** Active faulting in the Altyn Tagh - Karakorum junction area. (a) Simplified map of  
 83 Quaternary faults across western Tibet and Tarim (Karakax fault in red). Inset shows location  
 84 within India-Asia collision zone. Circles are epicenters of  $M \geq 5$  earthquakes since 1976 (SBX,  
 85 1997; USGS), colored as a function of depth. Dashed large white circles are reported or inferred  
 86 locations of older historical earthquakes. Black/white fault plane solutions are for  $M \geq 6.4$

87 *earthquakes recorded by [www.globalcmt.org](http://www.globalcmt.org), while two light-purple/white ones are those of the*  
88 *1882 and 1895 historical events, consistent with surface rupture observations (Liu, 1993). (b)*  
89 *Close-up of left-lateral Karakax fault main trace. Black square is location of Taersa terraces site.*  
90 *Thick yellow/red line shows ~150 km length of inferred sinistral surface rupture of 1882*  
91 *earthquake (black/white focal mechanism). Note ~80 km sinistral offset of Karakax river. Large*  
92 *white circles are Sites 1 and 4 from Peltzer et al. (2020) and small white circles refer to surface*  
93 *rupture field photographs and satellite images shown in Figure 12.*

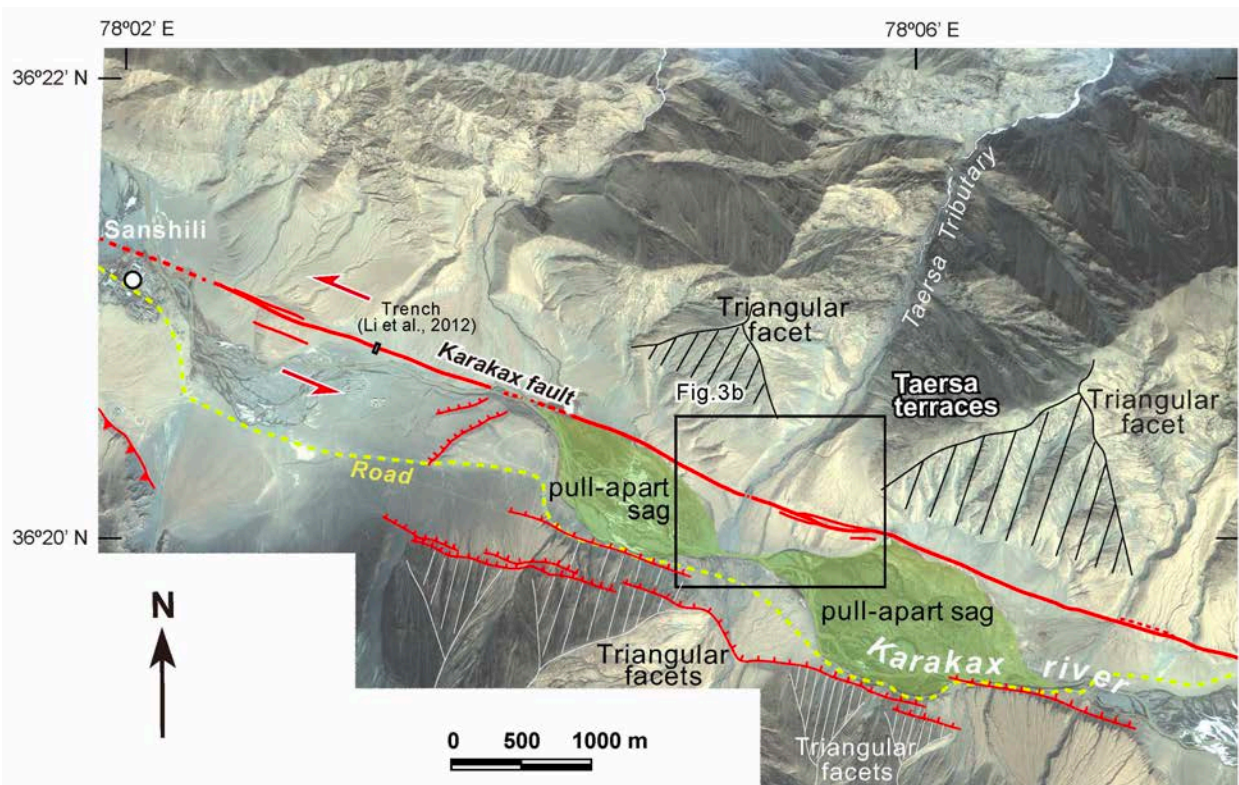
94

95       Pioneering observations with Landsat images demonstrated that the KXF is an active left-  
96 lateral strike-slip fault (Tapponnier and Molnar, 1977). The subsequent use of 10 m-resolution  
97 Spot images provided the first measurements of syn- or post-glacial offsets of up to 250 m  
98 (Peltzer et al., 1989). This initially suggested an inferred Holocene slip rate as large as ~20-24  
99 mm/yr, in keeping with the youthful geomorphic trace of the fault. Such a fast rate similar to that  
100 along California's San Andreas fault and compatible with that formerly inferred along the central  
101 ATF (~30 mm/yr, e.g., Molnar et al., 1987; Armijo et al., 1989; Molnar and Lyon-Caen, 1989)  
102 was long deemed plausible (e.g., Avouac and Peltzer, 1993; Avouac and Tapponnier, 1993). This  
103 was also consistent with a convergence rate between India and Asia formerly estimated to be as  
104 large as ~5 cm/yr based on Nuvel 1 and plate tectonic reconstructions (DeMets et al., 1990).  
105 Later on, quantitative field measurements and sampling suggested a slip rate bracket of 12-25  
106 mm/yr in the last ~115 ka (Ryerson et al., 1999; dataset published in Peltzer et al., 2020). Much  
107 slower slip rates, however, have been proposed in recent years. Li et al. (2012) suggested ~6-7  
108 mm/yr during the last ~1000 years, based on one <sup>14</sup>C age in a trench ~2 km east of Sanshili (Fig.  
109 2). At the location of our present study, from Optically Stimulated Luminescence (OSL) dating  
110 of fluvial sand samples from offset river terraces, Gong et al. (2017) obtained a similar rate of  
111 7.8±1.6 mm/yr during the last ~40 ka. Yet more recently, Peltzer et al. (2020) obtained an even



112 slower rate of  $2.6 \pm 0.5$  mm/yr since  $\sim 115$  ka, by combining diffusion modeling of fault scarps,  
 113 3D fan offset reconstructions, and OSL/ $^{10}\text{Be}$  dating of offset terraces at two sites  $\sim 35$  km apart  
 114 (Fig. 1b).

115 Here, based on Light Detection And Ranging (LiDAR) geomorphic measurements and  
 116  $^{10}\text{Be}/^{26}\text{Al}$  cosmogenic surface-exposure and depth profile dating at Taersa, 5 km east of Sanshili,  
 117 we further assess plausible values of the KXF slip rate in the last  $\sim 210$  ka and infer the return  
 118 times of four Holocene great earthquakes on the fault. This is possible because of the outstanding  
 119 preservation of superficial morphology due to a particularly arid climate (36 mm/yr of annual  
 120 precipitation in Kangxiwa, Yao et al., 1996). We also re-assess the  $\sim 150$  ka slip rate along the  
 121 Longmu Co fault,  $\sim 250$  km SE of the Karakax valley, and examine how such large faults control  
 122 the large-scale kinematics of block deformation across western Tibet.



123  
 124 **Figure 2.** Map of main active strands of Karakax fault system around Taersa site, based on  
 125 *Ikonos* image and field mapping of recent surface traces (red) across Karakax valley near

126 *Sanshili. The Taersa tributary flows south into a deep, swampy pull-apart sag (green shade)*  
127 *along the river valley, abandoning uplifted fans and terraces across the fault. Recent, north-*  
128 *facing and NE-striking normal fault scarps (red lines with tick bars) also cut fluvial fans south of*  
129 *the river. Triangular facets attesting to components of normal faulting south and north of the*  
130 *river are also indicated. Black rectangle shows location of trench site from Li et al. (2012).*

131

## 132 **2 Methods**

133 Meltwaters from the West Kunlun range glaciers flow into the ~EW-trending Karakax river  
134 valley (Fig. 2), depositing large fans and terraces (Fig. 3). The Karakax strike-slip fault, which  
135 runs parallel to the Karakax river, cuts and left-laterally displaces by tens to hundreds of meters  
136 most of these tributary landforms (Figs. 2 and 3). This ideal setting creates piercing points on  
137 each side of the fault that can be used to measure offsets, with assessable uncertainties thanks to  
138 the fairly linear geometry of the terrace risers.

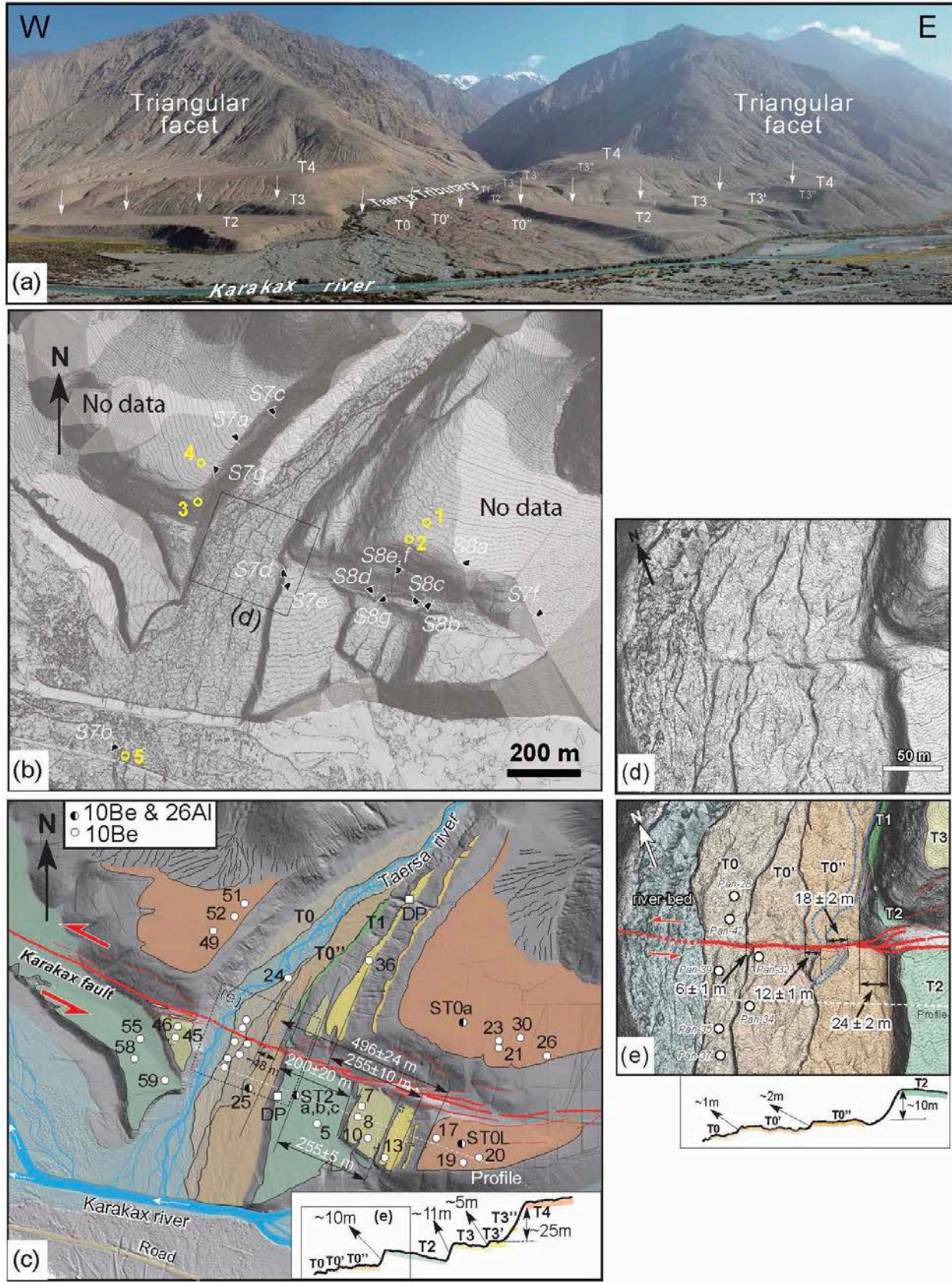
139 We combined field measurements and high-resolution satellite image interpretation to map  
140 active fault strands and offset geomorphic features, particularly within the Taersa paleo-fans and  
141 inset terraces (Fig. 3). In the field, using a tape, we first measured horizontal strike-slip offsets  
142 smaller than 30 m. We also used a Riegl VZ-1000 terrestrial LiDAR (angular resolution of 0.02°  
143 for raw data) to scan the Taersa fan and fan/terrace surfaces (five bases, Fig. 3b,d). After  
144 generating the point cloud using Riegl's "RiscanPro" software, we exported the data into "Global  
145 Mapper" to build a Digital Elevation Model (DEM) with a resolution of 0.5 m. We then  
146 extracted topographic profiles from the DEM and precisely measured cumulative horizontal and  
147 vertical fault offsets (Fig. 5). All DEM-derived measurements were compared with those directly  
148 measured in the field. Our high-resolution DEM, combined with the Ikonos satellite image of the  
149 entire Taersa site, was finally used to quantify the overall geometry of the fans and their offsets  
150 by the KXF (Figs. 5 and 6b).

151 At a more detailed level, we used the Matlab code “3D\_Fault\_Offsets” of Stewart et al.  
152 (2018) to measure the horizontal and vertical offsets of the youngest terrace risers (T0, T0', T0"  
153 and T2) (Figs. S1-S4). That code requires tracing of the fault on the DEM and identifying  
154 polygons to delineate terrace risers on both sides of the fault. Channel meandering along the  
155 various risers requires reducing the width of the polygons. The DEM uncertainties were set to be  
156 0.5 m, and 2 m for the position of the fault whose dip was taken to be  $70\pm 10^\circ$  (from trenching by  
157 Li et al., 2012).

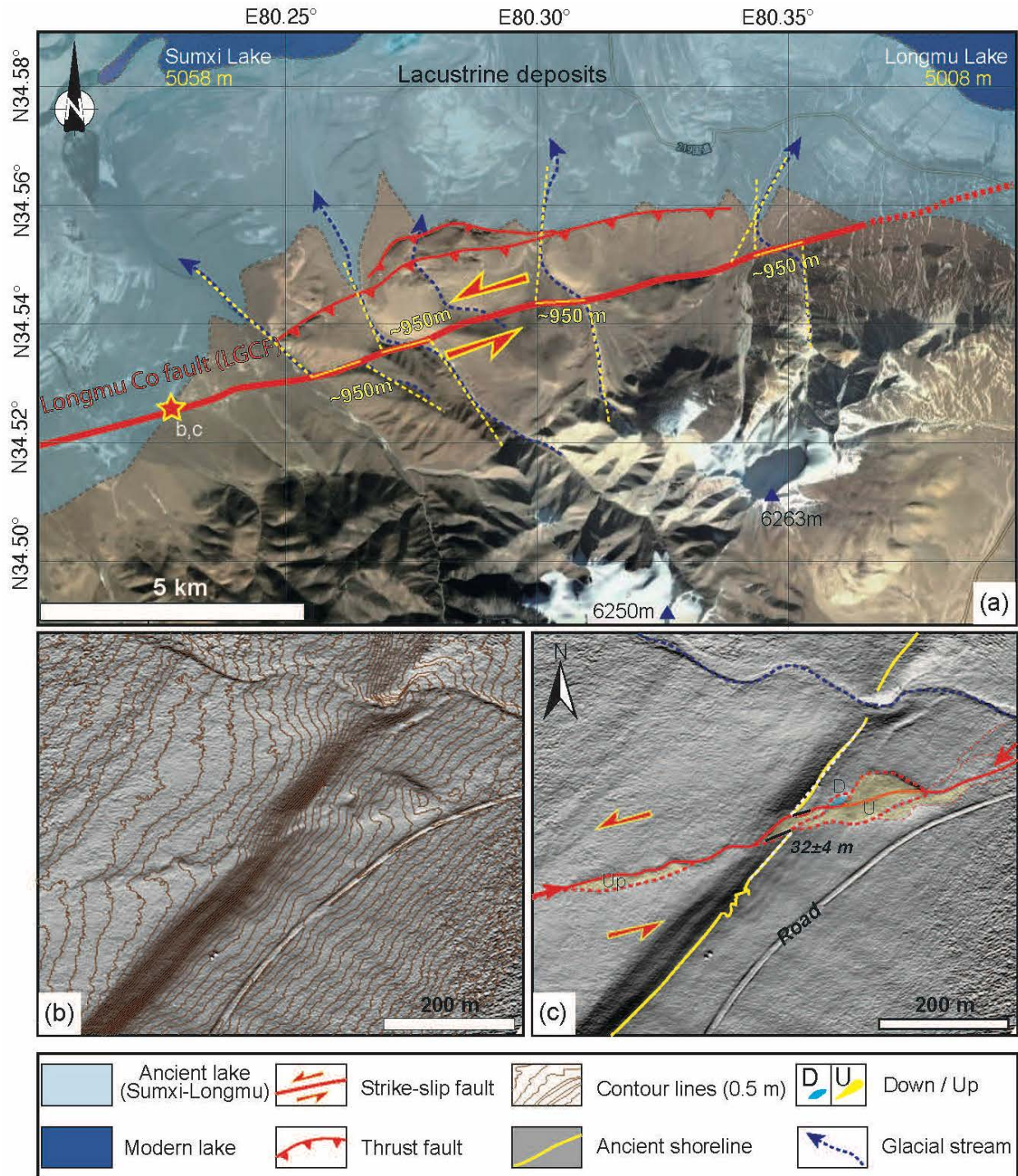
158 We also show in Figure 4 the DEM (9.78 cm/pix) that we recently obtained across the  
159 Longmu Co fault, where it offsets the highest shoreline of Sumxi-Longmu Lake (location in Fig.  
160 1a). That DEM was built by merging dozens of photos taken by our Unmanned Aerial Vehicle  
161 (UAV, DJI Phantom 4) using the software “Agisoft Metashape Professional”.

162 Our dating of fans and terraces at Taersa was based on the collection of a total of 35 quartz-  
163 rich cobbles (<25 cm in diameter) on the surfaces, as well as of nine samples in two depth  
164 profiles (down to ~140 cm) (Figs. 3, 8 and S5). From these samples, we obtained 35  $^{10}\text{Be}$  and six  
165  $^{26}\text{Al}$  cosmogenic model ages (Table 1). The clear desert varnish coating all the cobble surfaces  
166 (Figs. 8 and S5) (Farr and Chadwick, 1996), including on the lowest, youngest terraces, strongly  
167 suggests an absence of post-depositional reworking, and minimal rock weathering. The cobbles  
168 were crushed and sieved, and mineral separation and quartz cleaning were performed following  
169 standard procedures (e.g., Kohl and Nishiizumi, 1992).  $^{10}\text{Be}$  and  $^{26}\text{Al}$  model ages were calculated  
170 using the Lifton et al. (2014) ‘LSDn’ model in CRONUS version 3 (Balco et al., 2008) and are  
171 reported with  $1\sigma$  uncertainties (Table 1). The model ages from the two depth profiles were  
172 calculated using the Hidy et al. (2010) software (version 1.2).

173 We used statistical analyses based on Chauvenet's criterion (Bevington and Robinson, 2002)  
174 to discard potential outliers (including samples with excessive or insufficient  $^{10}\text{Be}$  or  $^{26}\text{Al}$   
175 concentrations) out of the age distributions. Slip rates during different time spans were then  
176 derived from the ranges of fan and terrace riser offsets and abandonment ages using the method  
177 of Zecher and Frankel (2009). We report the median rates (with uncertainties at the 68.27%  
178 confidence interval about the median) obtained using their Gaussian uncertainty model.  
179



181 **Figure 3.** Taersa terraces site: (a) View to NE of offset Taersa terraces and triangular facets.  
182 White arrows indicate main surface trace of Karakax fault. Note similar, maximum elevations of  
183 highest T4 fan surfaces on either side of the Taersa tributary valley. Location of photos in  
184 Figures S7 and S8 is indicated. (b and d) LiDAR DEM images (with 1 and 0.2 m contour lines,  
185 respectively), with (c and e) detailed field-based mapping of T0-T4 alluvial surfaces (colored)  
186 and seismic offsets, respectively. White areas in b are shielded from LiDAR surveys and five  
187 yellow circles show positions of survey bases. Small white circles (with numbers) indicate  
188 locations of dated cosmogenic surface samples. White squares labeled 'DP' are locations of  
189 depth profiles on T3' north of the fault and T2 south of the fault. Double arrows with numbers  
190 (in c) are apparent offsets of T4-T3'-T3 fan risers east of Taersa Holocene T0"/T0' fluvial  
191 channel (see text for details). Bottom right insets show profiles parallel to the fault (white dashed  
192 lines in c and e) across alluvial surfaces, extracted from LiDAR DEM. Single arrows with  
193 numbers (in e) point to single and cumulative co-seismic offsets of lowest T0 to T2 terrace risers.



194

195 **Figure 4.** Late Quaternary offsets along Longmu Co fault south of Sumxi-Longmu Lakes: (a)  
 196 Active trace of left-lateral fault and associated thrusts. Post-Marine oxygen Isotope Stage MIS-6  
 197 glacial valley offsets ( $950 \pm 50$  m) and location of offset of highest shoreline of paleo-Sumxi-  
 198 Longmu Lake are indicated by dashed blue lines and red star, respectively. (b) UAV-derived  
 199 DEM and (c) cumulative surface breaks and highest shoreline (~6 ka) offset (~32 m), with push-

200 *ups (Up, yellow shades) and pull-apart (Down, blue shade). Figure location is indicated in*  
201 *Figures 1a and 13a. See text for details.*

202

### 203 **3 Morphology, extent and offsets of the Taersa fans/terraces**

204 The Taersa site exposes four main alluvial fan and terrace surfaces (from T0, youngest, to  
205 T4, oldest), with several smaller, intermediate sub-levels (nine in total, Fig. 3). The broadest  
206 levels (T2, T3-T3' and T4) extend far on both sides of the Taersa tributary valley, north of the  
207 Karakax river. They correspond to three main generations of large interglacial fill-fans, that  
208 spread out broadly as the tributary reached into the main river valley. The curved, convex-  
209 upward, shapes of most of the uplifted terraces indicate that they correspond to conical alluvial  
210 fan surfaces (e.g., Meyer et al., 1996; Peltzer et al., 2020), which accounts for their slightly  
211 different elevations east and west of the tributary valley (Fig. 5b). Most of the other tributary  
212 streams have deposited similar imbricated alluvial fan surfaces along the Karakax valley (Li et  
213 al., 2012; Peltzer et al., 2020). The lowest/youngest terraces (T0, T0', and T0''), not far from the  
214 current river-bed, are covered with small boulders (<1 m in diameter, Figs. 8f,g and S5)  
215 deposited along recent, well-preserved braided channels (Fig. 3d). They are separated by small  
216 risers, 1-2 m-high at most (Figs. 3e and 5e). North of the fault, one additional young (low)  
217 terrace (T1) has been narrowly preserved (Fig. 3c,e), which we interpret to attest to the oblique  
218 component of footwall uplift north of the fault (Fig. 5a,c). Such uplift also promoted stronger  
219 lateral erosion of the upstream risers, hence affected their geometries more than that of their  
220 shielded counterparts south of the fault and east of the tributary (e.g., Cowgill, 2007; Gold et al.,  
221 2009; Mériaux et al., 2012).

222 The much smoother, higher fan surfaces T2-T4 are covered with fewer cobbles (Fig. 8b-e).  
223 South of the fault, their risers are higher than those of the T0s-T1 flight, from 5 to 25 m, up to a



224 maximum of 56 m above the present-day river-bed (Figs. 3c,e, insets and 5). North of the fault,  
225 that maximum height reaches  $\sim 70$  m (Fig. 5b). This shows that here, the Karakax main sinistral  
226 strand has a significant normal slip component, which we interpret to reflect extension along the  
227 northern edge of a pull-apart sag beneath the swampy meanders of the Karakax river east and  
228 west of Taersa (Fig. 2). Note that this pull-apart also corresponds to a southwestwards step where  
229 the main fault trace crosses the Karakax river from north to south. The pull-apart-related,  
230 extensional component has been long-lived since the cumulative vertical throw of fan surfaces  
231 T2 to T4 across the fault increases from 2 to 28 m (Fig. 5c). Also, the presence of triangular  
232 facets on both the north and south sides of the Karakax valley along mainly that stretch of the  
233 KXF supports long-term extension across that pull-apart sag (Figs. 2, S7f and S8f).

234 On the eastern side of the Taersa tributary floodplain, the T0'/T0 and T0''/T0' risers, one  
235 large fluvial paleo-channel within T0'', and the T2/T0'' riser (recall that T1 is not present south of  
236 the fault) are left-laterally offset by  $6\pm 1$ ,  $12\pm 1$ ,  $18\pm 2$ , and  $24\pm 2$  m, respectively (Fig. 3e), as  
237 measured in the field with a tape (Li et al., 2012). Note that the offsets of the channel axes and of  
238 the tops and bases of their bounding risers are indistinguishable and that, because of exceptional  
239 preservation due to the arid climate, the error bars on their offsets are generally on order of 10%.  
240 Using Stewart et al. (2018)'s "3D\_Fault\_Offsets" code, the corresponding, best-fitting horizontal  
241 offsets are  $5.9\pm 0.5$  m for T0/T0' (Fig. S1),  $12.8\pm 2.5$  m for the T0'/T0'' riser (Fig. S2),  $17.8\pm 1.5$   
242 m for the gully on T0'' (Fig. S3), and  $22.9\pm 1.5$  m for the T0''/T2 riser (Figs. S4, S6 and S7e)  
243 while vertical offsets are negligible ( $< 1$  m). The automatic restorations thus yield offsets that are  
244 consistent (at the 99% level) with our previous field and LiDAR survey measurements. The  
245 largest ( $\sim 23$ - $24$  m) offset is also found across several other Holocene fans and fan risers along  
246 the Karakax valley (Fig. 1b and Li et al., 2012).

247       The current left-lateral offsets of the higher/older T3/T2, T3'/T3 and T4/T3' riser bases and  
248 tops are  $200\pm 20$ ,  $255\pm 5$ , and  $255\pm 10$  m (Figs. 3c and S6) and  $196\pm 10$ ,  $255\pm 10$  and  $214\pm 10$  m  
249 (Fig. 5a), respectively. That the offset of the T4/T3' riser top ( $\sim 214$  m) is significantly smaller  
250 than that of the T3'/T3 riser ( $\sim 255$  m), which stands as much as 38 m down below T4 north of  
251 the fault (Fig. 5b), and therefore must be much younger, poses problem. This implies that, here,  
252 riser tops cannot simply be used to reliably measure cumulative offsets. One way to account for  
253 that puzzling observation is that greater incision associated with the vertical uplift north of the  
254 fault affected the now preserved apparent horizontal offsets. In addition, the presence of yet  
255 another, intermediate, barely preserved terrace ledge (T3'') between T4 and T3' (Figs. 3c, 5-8)  
256 implies that the total incision between the T4 and T3' levels was long-lived, and entailed several  
257 distinct episodes. Such long-lasting incision events likely broadened the valley width north of the  
258 fault at the T4 level by more than  $2 \times 70$  m (possibly as much as 258 m on the east side, Fig. 6a).  
259 North of the fault, this laterally eroded the currently narrow, remnant, footwall terrace ledges (T2,  
260 T3, T3' and T3''), and particularly the highest uplifted T4 fan riser. On the west side of the  
261 Taersa tributary, the more steeply incised valley edge ( $\sim 30^\circ$  east dip on average compared to  $\sim 18^\circ$   
262 west dip on average on the east side, Fig. 6a), likely accounts for the complete demise of all  
263 surfaces younger than T4, compared to the preservation of the east side ledges.

264       At a more detailed level, Figure 6b shows that the average slopes of the risers on the east  
265 side of the Taersa tributary decrease stepwise upwards from  $\sim 25^\circ$  to  $\sim 18^\circ$ , as their overall  
266 convexity increases with height, hence age, above river. This is consistent with the much greater  
267 degradation of the riser slopes north than south of the fault, which is clear on both the Ikonos  
268 imagery (Fig. 6c,d) and in the field (Fig. 8a). The composite T4/T3''/T3' riser, in particular, has  
269 been much more strongly incised by deeper and more numerous gullies perpendicular to the

270 Taersa tributary north than south of the fault (Figs. 6c,d and S7a). That the gullies south of the  
271 fault are narrower and shallower than those to the north is supported by the multiple yak/sheep  
272 paths that cross them, while none are observed to the north (Fig. 6c,d). Note that similar,  
273 asymmetric, fan/terrace aggradation and degradation processes have been described elsewhere  
274 along the eastern Altyn Tagh fault (e.g., Pingding Shan, Mériaux et al., 2012). Clearly, the strong  
275 erosional degradation of the highest, T4/T3' riser east of the Taersa tributary, and its correlative  
276 eastward retreat, make it challenging to use its present geometry to constrain a total cumulative  
277 offset in a traditional way.

278 In order to do so, one must factor in that the top offset must have been greater than apparent  
279 today (214 m, Fig. 5a). Before tectonic uplift and correlative river incision and valley widening  
280 north of the fault (Fig. 6a), the initial, upstream position of the top of the western riser of T4 east  
281 of the tributary (and to a lesser degree, possibly also of those of T3, T3' and T3'') must have  
282 been closer to the eastern edge of the Taersa tributary floodplain. A plausible position for the  
283 original western edge of T4 east of the tributary might have been between the present T0''/T0'  
284 and T1/T0'' risers, which mark the current minimum and maximum limits of that floodplain, ~48  
285 m apart (Fig. 3c). This would also be in keeping with the fact that the upstream Taersa tributary  
286 valley is deeply anchored, hence captive, within basement rocks that crop out on either side of  
287 the tributary valley almost all the way down to the KXF (Figs. 3a and S7). Consequently, the 214  
288 m apparent riser top offset of T4 might be increased to an average of  $496 \pm 24$  m (Figs. 3c and 7).

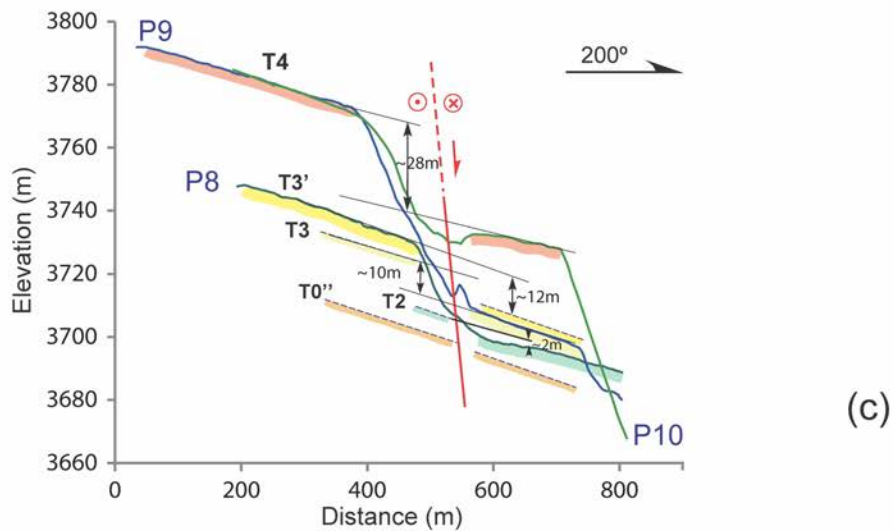
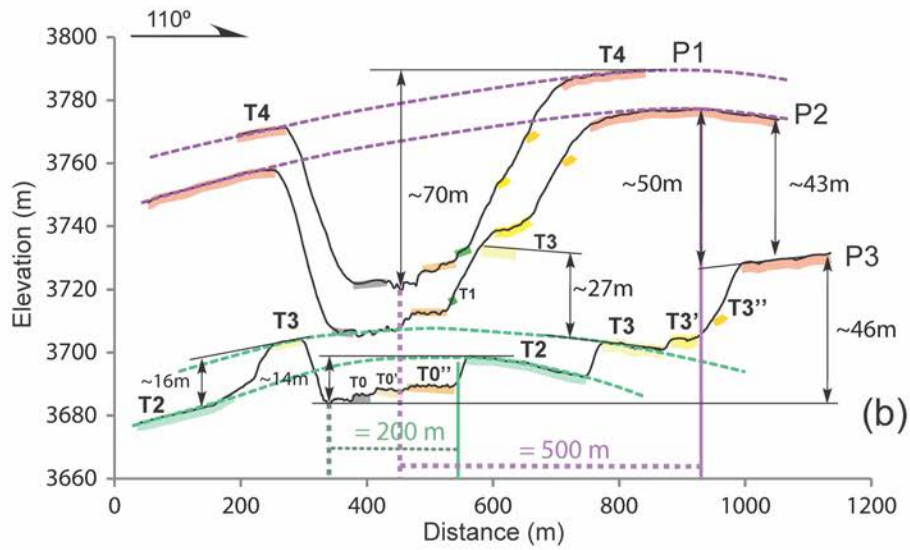
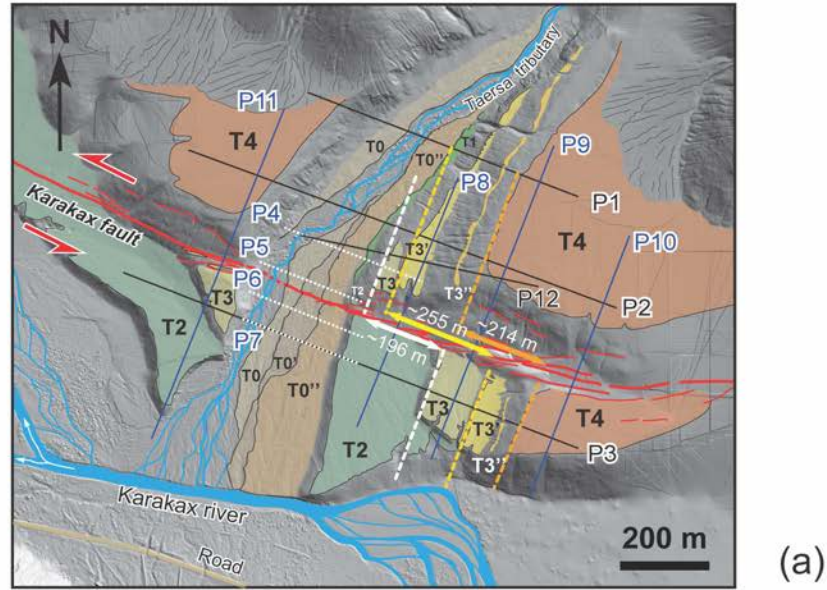
289 The two highest risers north and south of the fault are T4/T3' and T3/T2. The T3'/T3 riser,  
290 which is only ~3 to 5 m-high, compared to ~25 m for T4/T3' and ~12 m for T3/T2 (Fig. 5b),  
291 appears to be an intermediate feature, likely linked with a minor aggradation/incision change  
292 between the main climatic episodes that have shaped the Taersa tributary valley and alluvial fan

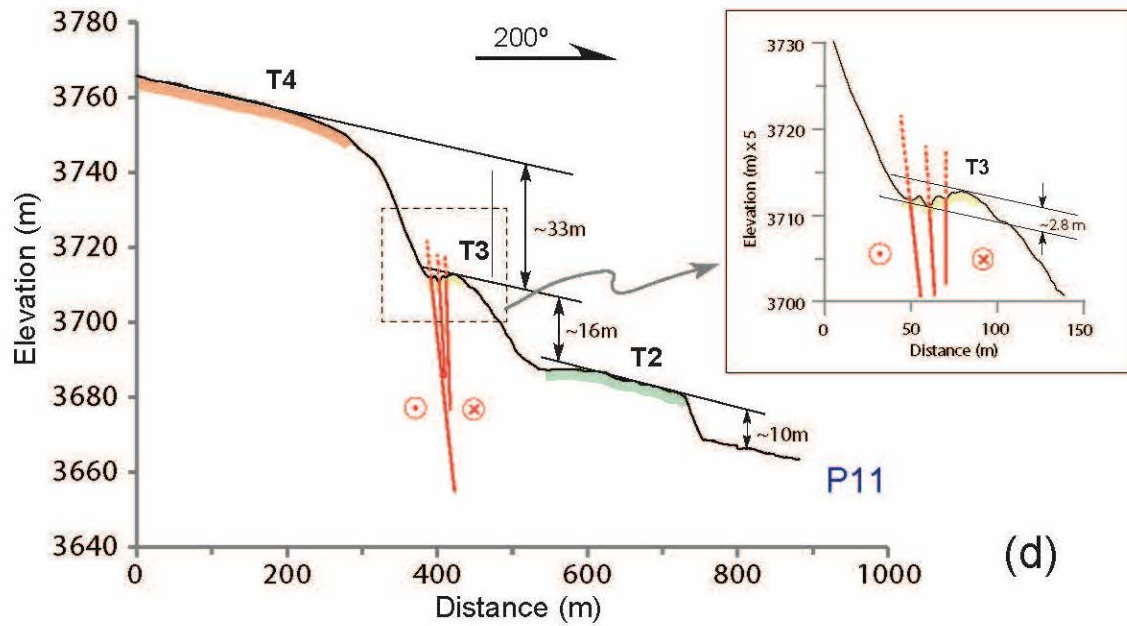
293 deposition. In addition, south of the fault trace, the T3'/T3 riser may have been degraded by the  
294 passage and recent incision of the large, mountain-sourced gullies that cross obliquely westwards  
295 most of the fan surfaces all the way to the Karakax river (Figs. S8 and S9). The fact that the  
296 T3'/T3 riser offset (indistinguishable top and base,  $255\pm 10$  m) is the same as that of the base of  
297 the T4/T3' riser, while their ages ought to be different, also poses problem. However, bearing in  
298 mind that T4/T3' and T3/T2 reflect the two major fan depositional events, coeval with the  
299 strongest glacial-interglacial transitions, the T3'/T3 offset value should nevertheless be taken  
300 into account.

301 The largest possible offset of the T4/T3' riser top ( $496\pm 24$  m) is comparable to that of the  
302 southeasternmost T4 fan outer limit along the Karakax river ( $\sim 500\pm 50$  m, Fig. 7a,b). That latter  
303 offset, as reconstructed in Figure 7a, also realigns the T4/T3' riser top south of the fault with the  
304 current eastern limit of the Taersa floodplain north of the fault (equivalent to the T0''/T0' riser),  
305 which independently validates the inference made regarding the initial position of that riser. As  
306 shown in Figure 7c,d, it is also possible to use 10 m-resolution, Tandem-X DEM data to assess in  
307 section the reconstruction of the initial T4 fan geometry. The best reconstructed fan shape  
308 corresponds to horizontal and vertical back-slip displacements of  $\sim 500\pm 50$  m and  $\sim 40\pm 10$  m,  
309 respectively. Such a  $\sim 500\pm 50$  m horizontal back-slip is the largest to still preserve a  $\sim 130$  m-  
310 wide passage for the Taersa tributary channel, broad-enough for it to flow between the T4W  
311 upstream and T4E downstream risers at the time ( $206\pm 25$  ka). This corroborates the inference  
312 that, on both its west- and southeast-facing limits, the original geometry of the T4 fan since  
313 abandonment has accrued approximately 500 m of sinistral offset along the KXF.

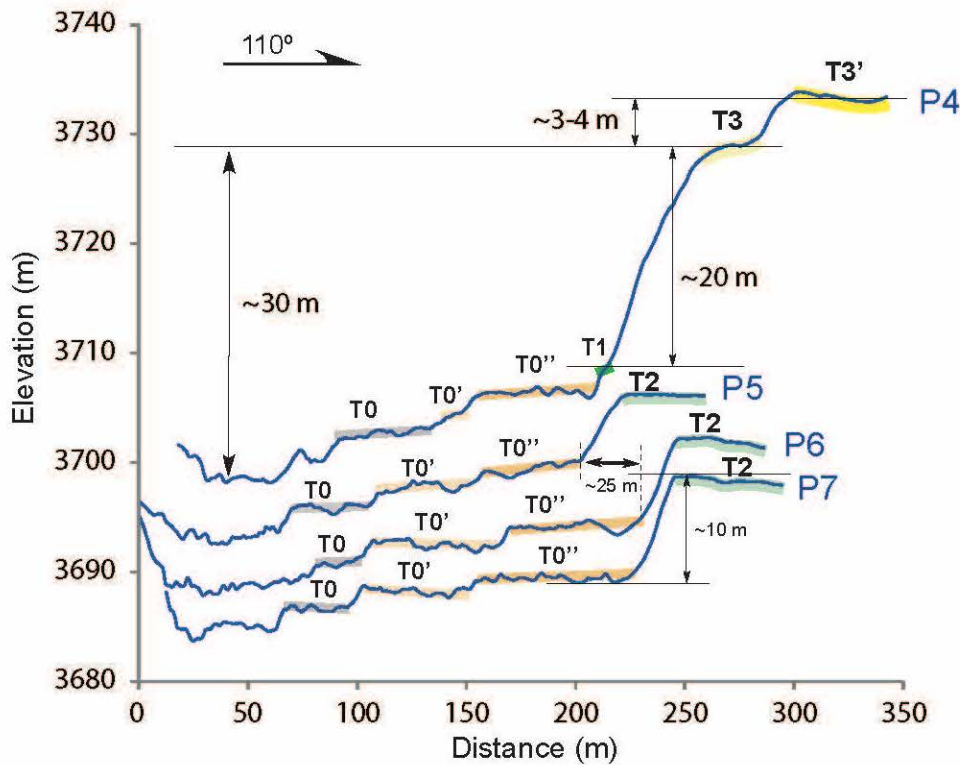
314            Lastly, it should be noted that the offset of the T3'/T3 riser at Taersa ( $\sim 255 \pm 10$  m) is  
315 commensurate with that of the corresponding Eemian T4 fan reconstruction ( $300 \pm 20$  m) at Site 4  
316 in Peltzer et al. (2020) located 18 km to the east (Fig. 1b).

317





(d)

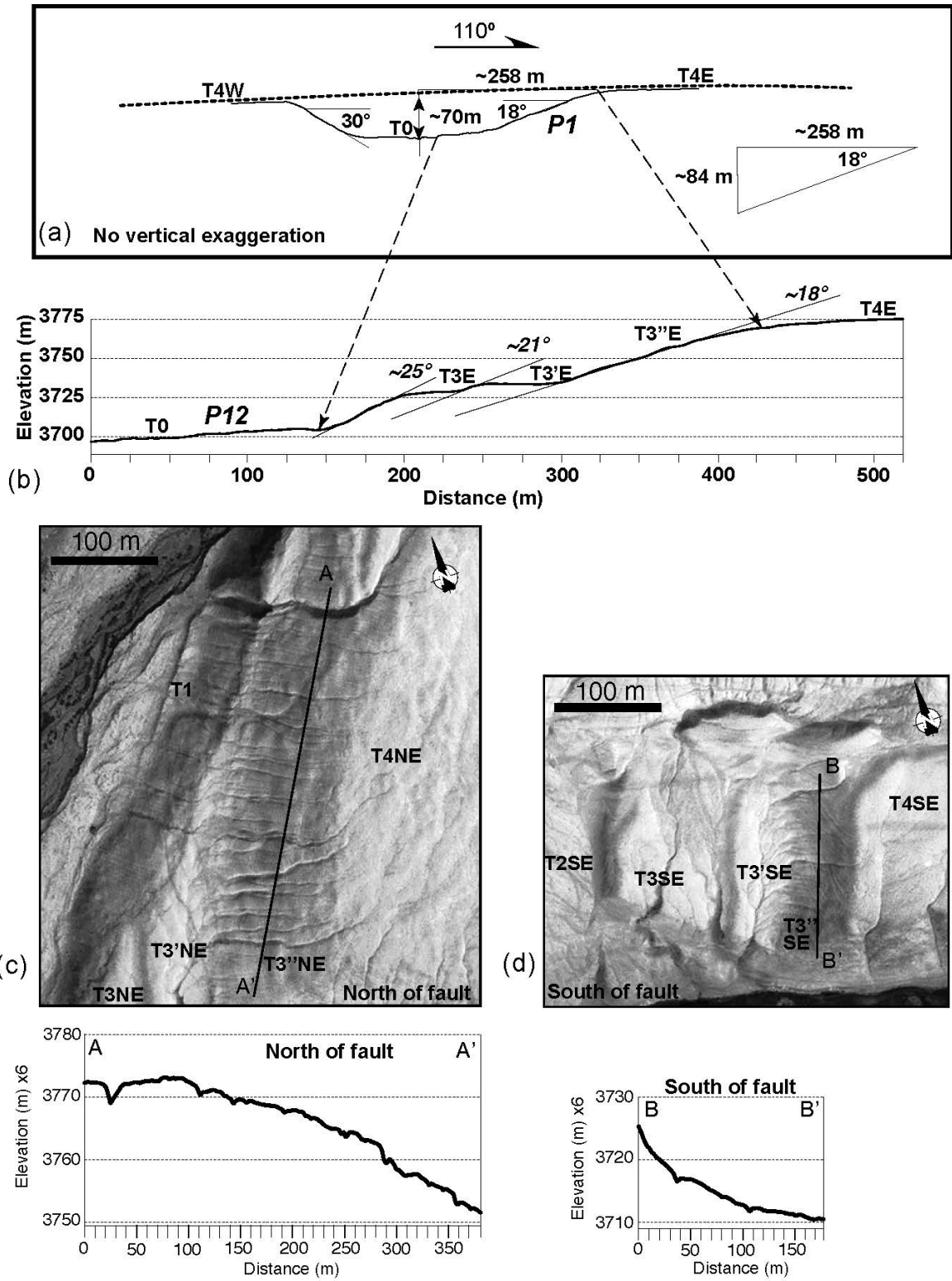


(e)

319  
 320 **Figure 5.** (a) Annotated LiDAR DEM of Taersa fan and terrace surfaces with location of  
 321 LiDAR-survey topographic profiles parallel (b and e) and perpendicular (c and d) to the  
 322 Karakax fault (vertical exaggeration x5). Note convex-upwards shape of profiles parallel to fault  
 323 (purple and green dashed lines), demonstrating fluvial fan origin of surfaces. Numbers indicate

324 *relative heights and distances between fan top (apex) and river bed (200 and 500 m), up- and*  
325 *downstream from the fault, respectively. Maximum cumulative co-seismic offset on T0'' (~25 m)*  
326 *is also indicated in (e). Note the uplifted, remnant shutter ridges (likely derived from the*  
327 *displacement of T4) in c (P9) and d (P11). Profile P12 is shown in Figure 6b.*  
328





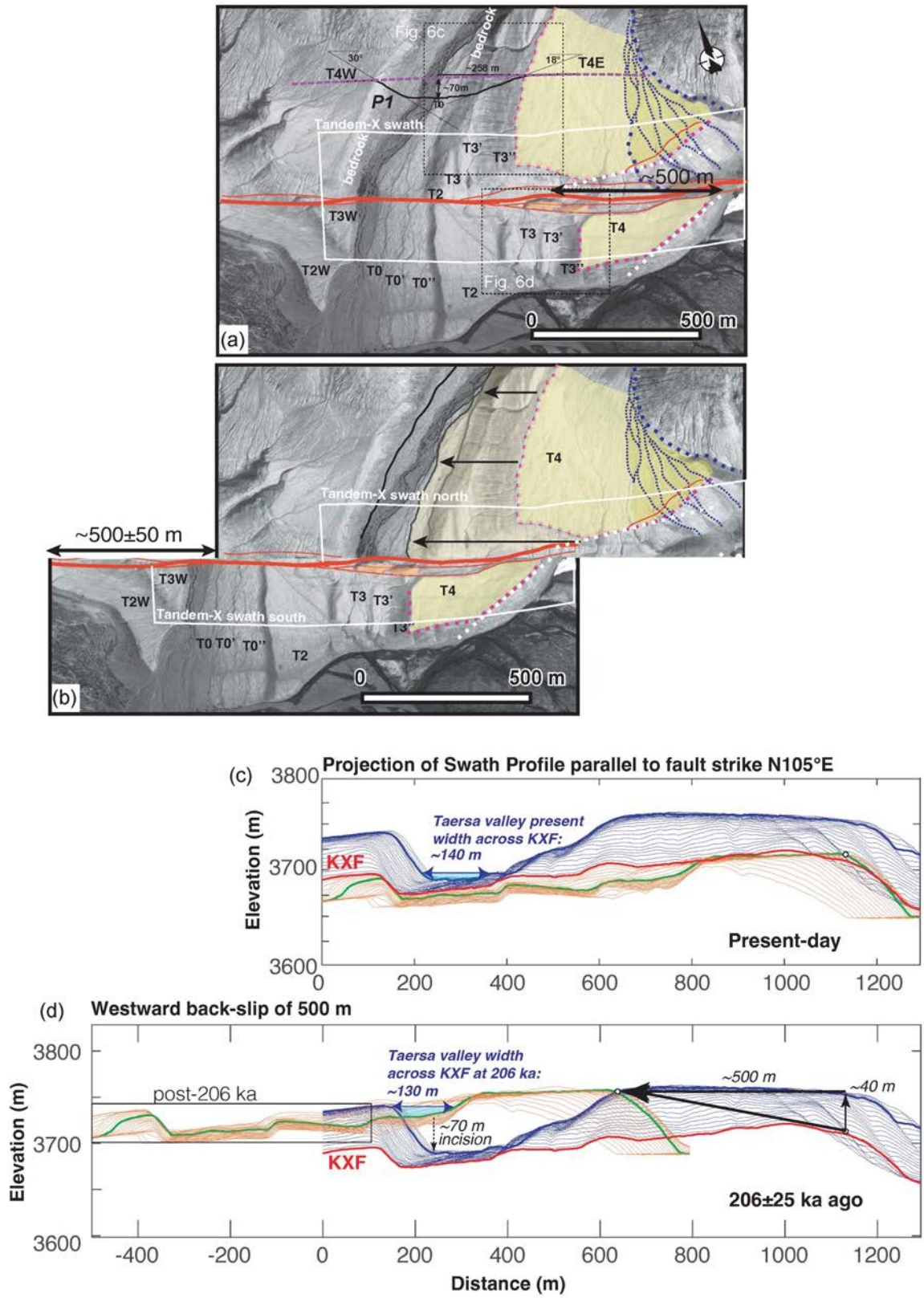
329

330

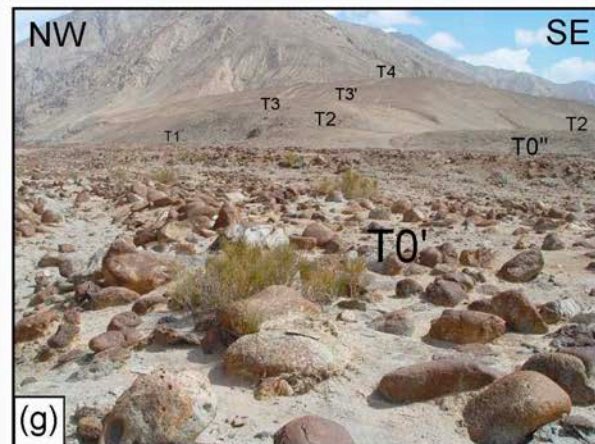
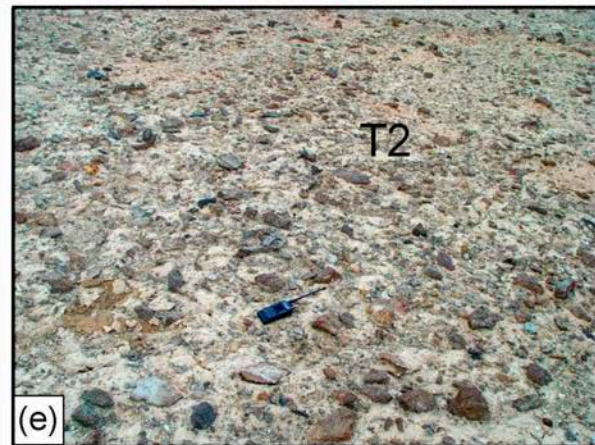
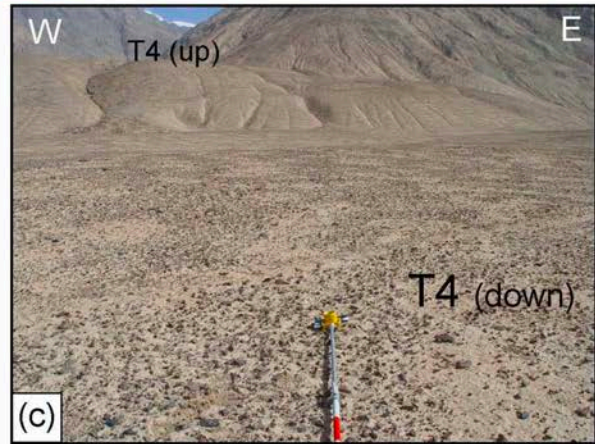
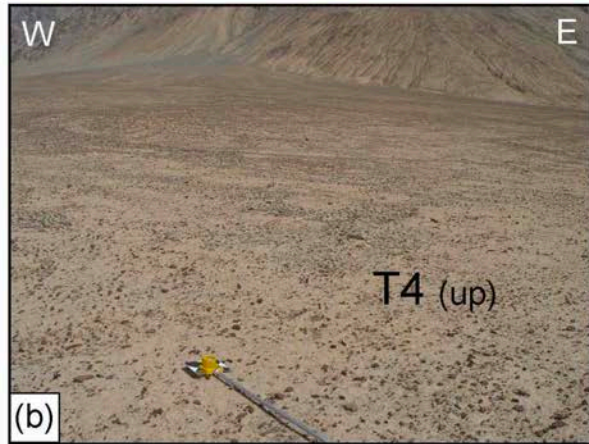
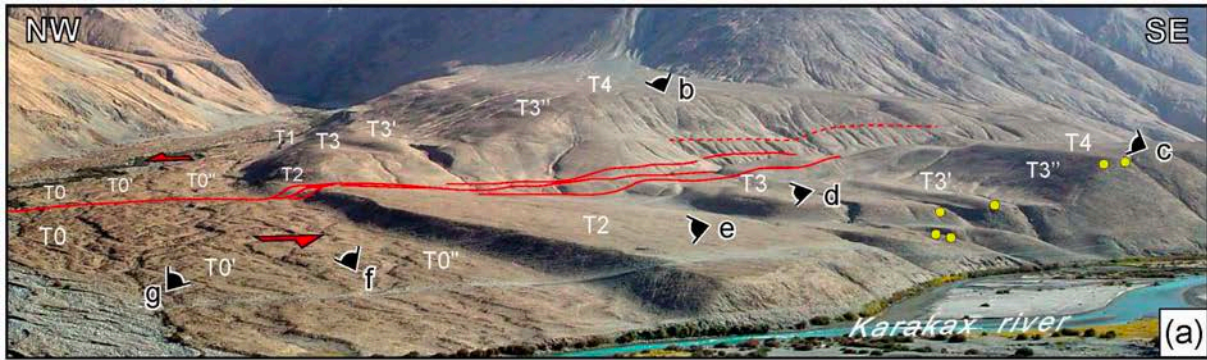
331

**Figure 6.** Morphology of the Taersa risers: (a) Profile P1 (see location in Fig. 5a) showing comparable elevations of T4E and T4W north of fault with incision depth of Taersa tributary,

332 *and average upstream valley slopes. (b) Higher resolution profile (P12 in Fig. 5a) showing step-*  
333 *wise steepening (18 to 25°) of average riser slopes ( $T4/T3'$ ,  $T3'/T3$ ,  $T3/T1$ ) as a function of*  
334 *younger age. (c and d) Close-up of Ikonos image (see location in Fig. 7a) showing varying*  
335 *degrees of rill incision on west-facing risers north and south of fault, respectively.*  
336



338 **Figure 7.** Reconstruction of the complete sinistral offset of oldest T4 fan surface taking into  
339 account normal component of uplift along left-lateral Karakax fault at Taersa site: (a) Ikonos  
340 image-based interpretation of T4 fan surface (pale yellow) including younger drainages to the  
341 east (on darker yellow fan). Position of profile in Figure 6a is indicated across upstream Taersa  
342 valley. East-west elongated, orange hills along main KXF trace (red) are shutter ridges likely  
343 derived from T4 (see also profiles in Fig. 5c,d). (b) Reconstruction of complete shape of T4 fan  
344 before uplift of T4north and incision of Taersa tributary north of fault, consistent with a  
345  $\sim 500 \pm 50$  m total offset of both western and southeastern edges of fan. See text for details. (c)  
346 Projection, along KXF at Taersa, of 400 m-wide topographic profiles swath (20 south of fault,  
347 red; 20 north of fault, blue) from Tandem-X DEM (vertical exaggeration x2). Red line is KXF  
348 fault trace. Thick dark blue line is present envelope of highest surface (T4) across Taersa valley  
349 (light blue shade) north of fault. Thick green line is present envelope of highest surfaces (T4-T3'-  
350 T3) across Taersa valley south of fault. (d) Reconstruction of  $\sim 500$  m westward back-slip (as in b)  
351 of red profiles south of fault (vertical exaggeration x2). Note preservation of  $\sim 130$  m-wide valley  
352 width across fault at  $\sim 206$  ka, similar to present valley width ( $\sim 140$  m). Black vectors to the right  
353 indicate vertical and left-lateral offsets across KXF since 206 ka.



355 **Figure 8.** *Field photographs of Taersa fan and terrace surfaces (a) showing distinct cobble*  
356 *sizes and surface roughness as a function of abandonment age north (b) and south (c-g) of the*  
357 *fault. The younger the surface the larger and coarser the samples, as expected. Yellow circles*  
358 *indicate locations of Optically Stimulated Luminescence (OSL) samples from Gong et al. (2017).*  
359 *See text for discussion.*

360

#### 361 4 $^{10}\text{Be}$ , $^{26}\text{Al}$ cosmogenic surface and depth profile dating of the alluvial

#### 362 surfaces

363 The ages of the 35 samples dated on the alluvial surfaces along either sides of the fault and  
364 Taersa tributary valley (Fig. 3c) are shown in Table 1 and plotted in Figure 9.

365 The youngest  $^{26}\text{Al}$  age on T4 may be statistically rejected as a clear outlier, using Chauvenet  
366 criterion, while the 13 remaining ages (12  $^{10}\text{Be}$  and one  $^{26}\text{Al}$  on both T4E and T4W) range  
367 between 162 and 245 ka, with an average of  $206 \pm 25$  ka ( $1 \sigma$ ). This confirms that the highest T4  
368 surfaces belong to the same large fan on both sides of the Taersa tributary. Note that the T4  
369 alluvial surface dated at Taersa (the oldest age is  $245 \pm 16$  ka) is amongst the oldest ever dated in  
370 and along the margins of Tibet (e.g., Hetzel et al., 2002; Blisniuk and Sharp, 2003; Tao et al.,  
371 2020). This attests that regional erosion of the surface tops is minimal, as previously suggested in  
372 other areas of NE Tibet (e.g., Hetzel et al., 2002).

373 The two sample ages on T3' (191 and 215 ka) yield an average age of  $203 \pm 18$  ka,  
374 comparable to that of T4. The narrow widths of T3', at the base of the high T4/T3' risers that  
375 bound the west sloping surfaces of T4 (Fig. 3c), suggest that both samples might have foundered  
376 from T4, likely due to co-seismic shaking. High-resolution satellite images and broad-scale field  
377 photograph (Fig. 8a) confirm that much of the T4/T3' riser slope is covered with large boulders  
378 that have toppled down during rockfalls. This likely accounts for their apparently similar ages,  
379 despite the large elevation difference ( $\sim 43$ -50 m north, and  $\sim 25$  m south of the fault, Fig. 5b).

380 The age distribution on T3 is completely different east and west of the Taersa tributary (Fig. 9).  
381 To the east, the concordant average ages of the three samples is  $185\pm 2$  ka, a value roughly  
382 consistent with the average ages on T3' and T4. We thus infer that they were similarly  
383 transported out of T4, likely along the large south-flowing gullies that drain it (Figs. S8 and S9).  
384 To the west, by contrast, the two samples collected on the surface of the small remnant of T3,  
385 which is separated from T4 by a  $\sim 2$ - $3$  m-deep sag along the fault (Figs. 3 and 5d), have much  
386 younger ages ( $97\pm 6$  and  $127\pm 8$  ka) (Fig. 9). Such  $\sim 100$  ka-younger ages are consistent with the  
387 elevation differences between T4 and T3 ( $\sim 33$  m, Fig. 5d), or T3 and T0 ( $\sim 26$  m, Fig. 5d) on the  
388 Taersa tributary west bank. These ages are also similar to those found by Peltzer et al. (2020) on  
389 their highest surfaces (T4)  $\sim 30$  m above the local tributary at their Site 4. Hence, although we  
390 have only two in situ ages for now, we infer that the average age ( $112\pm 21$  ka) of our two samples  
391 on T3W represents the actual age of the Taersa T3-T3' surfaces. At a more detailed level, one  
392 might further hypothesize that the small,  $\sim 3$ - $5$  m-high riser between T3 and T3' east of the  
393 Taersa tributary corresponds to that observed by Peltzer et al. (2020)'s between their T3 and T4  
394 surfaces at their Site 4. In that case, the T3 and T3' fan surfaces at Taersa would be even closer  
395 in age ( $97\pm 6$  and  $127\pm 8$  ka) with those dated farther east ( $\sim 95.9\pm 2.8$  and  $112.9\pm 6.5$  ka). It is  
396 clear, however, that additional sampling would be needed to confirm that inference.

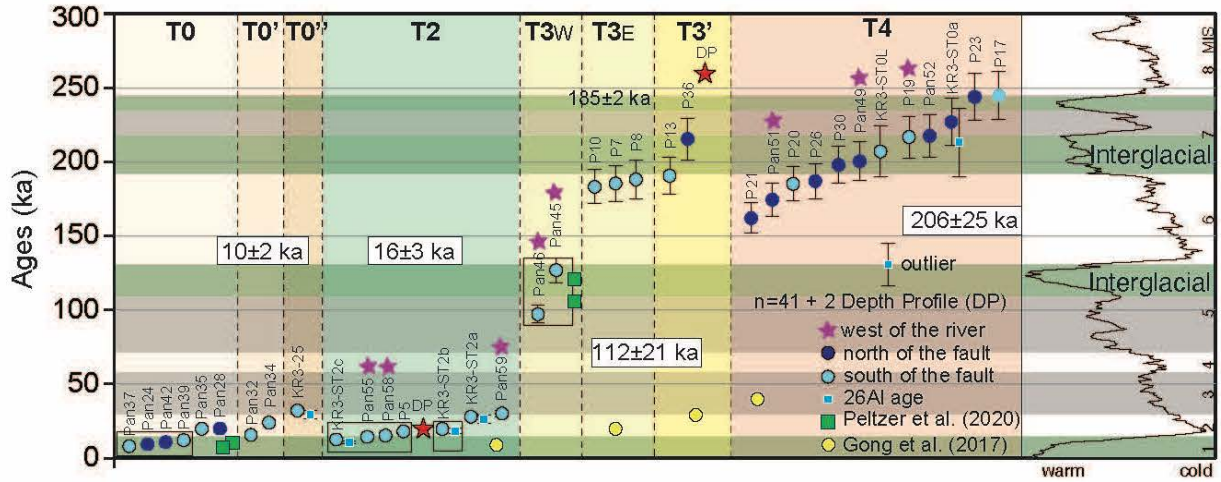
397 At the level of T3' north of the KXF, one depth profile was retrieved from a refreshed riser  
398 in a deep incision that reaches the top of T4 (Figs. 3c and S7). Four individual cobbles collected  
399 between 55 and 120 cm-depths yield consistent  $^{10}\text{Be}$  and  $^{26}\text{Al}$  model ages of  $\sim 260$  and  $\sim 256$  ka  
400 (Fig. 10). Such ages, however, are  $\sim 50$  ka older than the average age ( $\sim 206$  ka) of the T4 surface  
401 above, which is stratigraphically puzzling. They might be interpreted to date reworked colluvium

402 derived from the erosion of surfaces higher than T4, upstream along the Taersa tributary. In any  
403 case, these old ‘inherited’ ages must predate the abandonment of either T3’ or T4.

404 On T2, which is well-preserved only south of the fault, ten surface sample ages (seven  $^{10}\text{Be}$   
405 and three  $^{26}\text{Al}$ ) fall between 11 and 30 ka, with an average age of  $19\pm 7$  ka. Three ages ( $\sim 28\pm 2$  ka  
406 on average), are significantly older, by  $\sim 10$  ka, than the majority of the seven others (average of  
407  $16\pm 3$  ka). One depth profile in the refreshed eastern T2/T0” riser (Fig. S5) yields model  $^{10}\text{Be}$  and  
408  $^{26}\text{Al}$  surface ages between 11 and 20 ka (average of  $15.5\pm 4.5$  ka), after rejection of two clear  
409 outliers (Fig. 10). Such concordant ages confirm that T2, which fans out of the Taersa gorge into  
410 the Karakax valley, is best interpreted as a fan-shaped fill terrace, resulting from post-glacial  
411 melting.

412 The morphologies of the lowest terraces (T0-T0’-T0”), that stand 10 m below T2 but only  
413 1-2 m above each other and the present-day river bed, are similar, with remarkably well-  
414 preserved braided channels (Figs. 3d,e, 5e and S7b). They must therefore be significantly  
415 younger than T2 ( $\sim 16$  ka). The unique sample on T0”, with ages of 32 ka ( $^{10}\text{Be}$ ) and 29 ka ( $^{26}\text{Al}$ )  
416 (average of  $31\pm 2$  ka) must thus be an outlier derived from erosion of T2. Likewise, the two  $^{10}\text{Be}$   
417 samples on T0’ (16 and 24 ka with an average of  $20\pm 6$  ka) must also be outliers derived from T2.  
418 Finally, the six samples on T0 include two  $\sim 20$  ka and four  $10\pm 2$  ka ages, consistent with  
419 inheritance of the two older cobbles, while the youngest majority reflects T0’s actual Holocene  
420 age.





421  
 422 **Figure 9.** Ages at the Taersa site.  $^{10}\text{Be}$  and  $^{26}\text{Al}$  surface-exposure cosmogenic ages (numbered  
 423 as in Fig. 3c,e and Table 1) using the Lifton et al. (2014) 'LSDn' model in CRONUS version 3,  
 424 with  $1\sigma$  uncertainties. Ages in white boxes are average of all individual ages for T4, and average  
 425 of ages in thin black boxes for T3W, T2 and T0. Green squares refer to ages from Site 4 in  
 426 Peltzer et al. (2020) (location in Fig. 1b). Yellow circles are OSL ages from Gong et al. (2017).  
 427 Right panel shows global climatic proxy curve of Lisiecki and Raymo (2005), with grey-shaded  
 428 sectors indicating Marine oxygen Isotope Stages (MIS) 1 to 8. Green bands are interglacial  
 429 periods, during which glaciers melt coeval with deposition of large alluvial fans and terraces.  
 430 See text for details.

431  
 432 **Table 1:** Analytical results of  $^{10}\text{Be}$  and  $^{26}\text{Al}$  geochronology and surface-exposure model ages at  
 433 Taersa site along Karakax fault.

Surface	Sample name	Lat (N)	Long (E)	Elev (m)	Depth (cm)	Quartz (g)	Be carrier (mg)	Al carrier (mg)	$^{10}\text{Be}/^{26}\text{Al}^{27}$ ( $10^{-15}$ )	$^{10}\text{Be}$ ( $10^6$ atom/g)	$^{26}\text{Al}$ ( $10^6$ atom/g)	Lm (+ ext. uncert.)	LSDn (+ ext. uncert.)	(int. Uncert.)	(int. Uncert.)
T0SE	KXW-Pan 39*	36.33562	78.08641	3711	0	20.4503	0.3464	/	450±8	0.509±0.009	/	12155±945	237	<b>12155±758</b>	237
	KXW-Pan 35*	36.3352	78.0863	3707	0	20.050	0.3461	/	783±10	0.903±0.012	/	20261±1555	279	<b>19751±1204</b>	272
	KXW-Pan 37*	36.33505	78.0863	3706	0	20.112	0.3465	/	276±7	0.318±0.008	/	7908±628	201	<b>8059±519</b>	205
	KXW-Pan 24**	36.33717	78.08839	3729	0	26.138	0.3799	/	379±12	0.368±0.012	/	9138±750	299	<b>9366±633</b>	307
T0NE	KXW-Pan 28**	36.33619	78.08708	3720	0	25.267	0.3774	/	919±26	0.917±0.026	/	20414±1651	592	<b>19881±1314</b>	577
	KXW-Pan 42**	36.33612	78.08694	3719	0	24.964	0.3796	/	421±14	0.428±0.014	/	10524±871	361	<b>10716±733</b>	368
T0'SE	KXW-Pan 32*	36.33569	78.08686	3716	0	20.130	0.3464	/	614±8	0.706±0.009	/	16066±1232	224	<b>15737±959</b>	219

	KXW- Pan 34*	36.33534	78.08664	3710	0	20.101	0.3455	/	991± 14	/	1.138±0.016	/	24867±1914	355	<b>23934±1464</b>	342	
	KR3-25								921±								
T0'SE	\$	36.33441	78.08694	3710	0	15.008	0.4259	/	17	/	1.79±0.049	/	33792±2731	941	<b>32046±2109</b>	892	
									2.2233	/	2815± 106	/	9.639 ±0.37 2 26Al: 29973±3099	1177	<b>26Al: 29475±2826</b>	1157	
T2SE	KXW- P5**	36.33336	78.0889	3714	0	25.657	0.3801	/	824± 19	/	0.816±0.019	/	18407±1457	440	<b>17994±1151</b>	430	
	KR3- ST2-a	\$	36.33433	78.08817	3710	0	15.848	0.4395	/	16	/	1.56±0.044	/	29182±2359	824	<b>27902±1839</b>	787
									2.1199	/	2745± 89	/	8.518 ±0.35 9 26Al: 26577±2780	1137	<b>26Al: 26195±2547</b>	1121	
	KR3- ST2-b	\$	36.33433	78.08817	3710	0	15.183	0.4376	/	11	/	1.041±0.029	/	20158±1625	569	<b>19655±1292</b>	555
									7.7873		473±2 5	/	5.635 ±0.29 9 26Al: 18274±1993	979	<b>26Al: 18406±1879</b>	986	
	KR3- ST2-c	\$	36.33433	78.08817	3710	0	15.154	0.4361	/	6	/	0.616±0.018	/	12618±1016	360	<b>12583±827</b>	359
									2.5932	/	320± 716±3 3	/	2.841 ±0.14 8 26Al: 10096±1091	529	<b>26Al:10588±1071</b>	555	
DP T2	KR3-3	\$	36.33433	78.08817	3710	50	15.006	0.4364	2.6239	1027	2614± ±20	95	1.998±0.056	22	/	/	/
	KR3-12	\$	36.33433	79.08817	3710	106	15.126	0.6625	1.1776	312±	2565±	11	0.916±0.037	1	/	/	/
	KR3-13	\$	36.33433	80.08817	3710	110	15.106	0.6573	2.4222	372±2	87±4	4	0.254±0.013	9	/	/	/
	KR3-18	\$	36.33433	81.08817	3710	130	15.389	0.6546	2.0230	286±3	53±2	1	0.15±0.007	3	/	/	/
	KR3-20	\$	36.33433	82.08817	3710	140	13.499	0.4570	0.9900	714±4	92±3	1	0.208±0.008	2	/	/	/
T2SW	KXW- Pan 55**	36.33561	78.08362	3705	0	25.572	0.3786	/	640± 20	/	0.633±0.02	/	14634±1202	477	<b>14405±975</b>	470	
	KXW- Pan 58**	36.33506	78.08346	3699	0	27.118	0.3784	/	726± 23	/	0.677±0.021	/	15577±1279	506	<b>15292±1034</b>	497	
	KXW- Pan 59**	36.33455	78.08461	3703	0	25.830	0.3783	/	1493 ±47	/	1.461±0.046	/	31770±2615	1019	<b>30135±2039</b>	966	
T3SE	KXW- P8**	36.33362	78.09042	3717	0	6.862	0.3734	/	2535 ±75	/	9.221±0.275	/	199175±17190	6351	<b>188071±13245</b>	5975	
T3SE	KXW- P7**	36.33354	78.09035	3716	0	20.886	0.2935	/	9683 ±176	/	9.118±0.166	/	195720±16139	3812	<b>185330±12184</b>	3597	
T3SE	KXW- P10*	36.33332	78.09059	3714	0	20.008	0.3277	/	8148 ±54	/	8.917±0.059	/	193279±15530	1376	<b>183143±11565</b>	1300	
T3SW	KXW- Pan 46*	36.33608	78.08486	3724	0	20.106	0.3461	/	4079 ±23	/	4.692±0.026	/	101486±7897	596	<b>97092±5945</b>	570	
T3SW	KXW- Pan 45**	36.33597	78.08498	3721	0	16.5205	0.3794	/	4126 ±96	/	6.331±0.1476	/	135174±11109	3298	<b>126805±8394</b>	3085	
T3'SE	KXW- P13**	36.33289	78.09108	3711	0	22.405	0.3793	/	8259 ±111	/	9.343±0.125	/	202703±16535	2920	<b>190625±12299</b>	2735	
T3'NE	KXW- P36**	36.33745	78.09018	3758	0	25.269	0.3797	/	1086 1±14	/	10.905±0.142	/	232977±19185	3293	<b>215461±14000</b>	3028	
DP T3'	KR3-29	\$	36.33921	78.09165	3770	55	12.7368	0.3639	2.1456	4331	10441	±58	±361	8.279±0.199	06	/	/
	KR3-31	\$	36.33921	79.09165	3770	100	35.0026	0.4584	1.7434	5883	25547	±84	±771	5.155±0.127	05	/	/
	KR3-33	\$	36.33921	80.09165	3770	110	20.8226	0.3026	2.0375	3820	8206±	±74	235	3.715±0.103	01	/	/
	KR3-34	\$	36.33921	81.09165	3770	120	24.5691	0.2943	5.9325	4910	3497±	3	3.935±0.129	19.33	/	/	

	§								±128	112		5±0.6					
												27					
T4SE	KXW-P20*	36.33283	78.09419	3740	0	20.372	0.3272	/	8540	/	9.165±0.063	/	195637±15738	1455	<b>185071±11701</b>	1371	
	KXW-P17**	36.33317	78.09257	3733	0	25.926	0.3796	/	1231	/	12.046±0.161	/	263775±21969	3870	<b>244714±16081</b>	3567	
	KXW-P19**	36.33271	78.09392	3736	0	25.267	0.3794	/	4±16	/	10.82±0.145	/	234059±19299	3411	<b>216647±14103</b>	3139	
	KR3-STOL §	see map	see map	3740	0	15.110	0.4376	/	1078	/	11.998±0.596	/	222489±21572	11912	<b>206956±17113</b>	11022	
									6192								
									±281								
									2.3834	/			43.57				
									11867	/			2±2.3		26Al:		Al26:
									±519	/			76	135936±15988	8022	<b>130901±14384</b>	7702
T4NE	KR3-ST0a §	see map	see map	3790	0	15.001	0.4363	/	6927	/	13.482±0.373	/	245894±21358	7397	<b>226885±15962</b>	6781	
									2.3458	/			71.05				
									19579	/			2±2.9		26Al:		26Al:
									±511	/			34	223583±26172	10525	<b>213150±23039</b>	9972
	KXW-P30*	36.3356	78.09543	3786	0	20.265	0.3288	/	9412	/	10.206±0.07	/	213090±17244	1591	<b>197897±12566</b>	1470	
	KXW-P21**	36.3347	78.09499	3771	0	24.5581	0.379	/	7936	/	8.185±0.1112	/	173423±14011	2497	<b>161960±10354</b>	2323	
	KXW-P23**	36.33473	78.09479	3771	0	24.965	0.3797	/	1208	/	12.276±0.159	/	263360±21912	3751	<b>243802±15993</b>	3449	
	KXW-P26**	36.33454	78.09664	3748	0	26.150	0.3791	/	0±15	/	9.326±0.123	/	198063±16122	2794	<b>186999±12039</b>	2628	
	KXW-Pan 52**	36.33884	78.08673	3776	0	26.497	0.3796	/	9626	/	11.119±0.199	/	235556±19665	4571	<b>217467±14428</b>	4194	
	KXW-Pan 49**	36.33823	78.08601	3769	0	17.922	0.2912	/	1161	/	10.299±0.166	/	215554±17790	3754	<b>200287±13112</b>	3470	
	KXW-Pan 51**	36.33906	78.08698	3778	0	18.749	0.2906	/	6±20	/	8.856±0.145	/	185259±15142	3242	<b>174411±11330</b>	3041	

Samples “\*” and “\*\*” were collected in 2011 and processed at Stanford University's cosmogenic facility and samples “§” were collected in 1995 and processed and measured at Center for Accelerator Mass Spectrometer (CAMS) at Lawrence Livermore National Laboratory (LLNL).

<sup>10</sup>Be/<sup>9</sup>Be ratios “\*” were measured at CAMS at LLNL and <sup>10</sup>Be/<sup>9</sup>Be ratios “\*\*” measured at ASTER (CEREGE).

Ages calculated with the CRONUS 3 calculator (Balco et al., 2008). Lm= Lal (1991)/Stone (2000) time-dependent production rate model. LSDn = Lifton et al. (2014) model ages discussed in text.

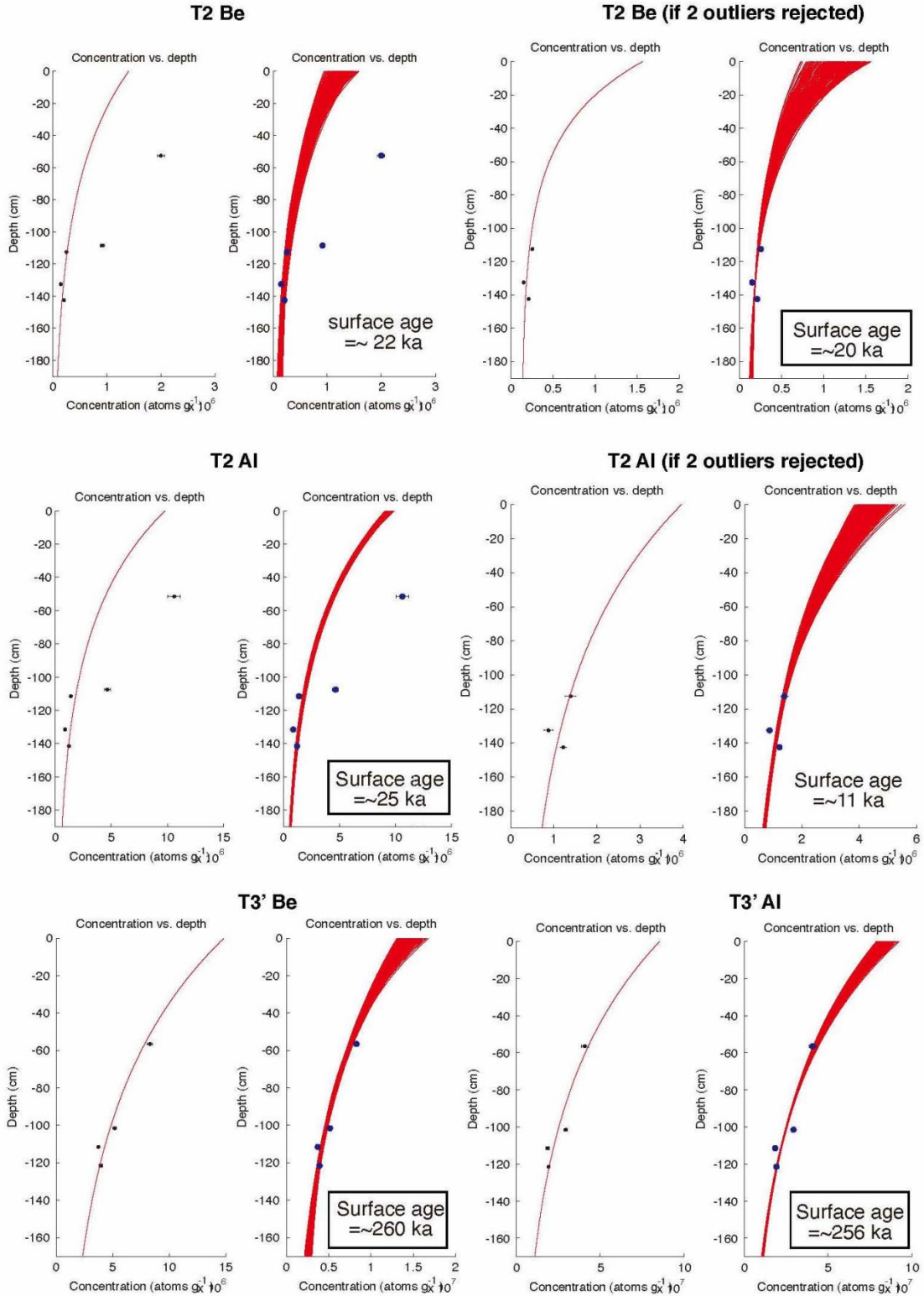
“See map” refers to Figure 3c, because no exact GPS location was measured in the field.

Shielding factor is 0.98; Sample density is 2.65 g/cm<sup>3</sup> (all samples are quartzite). Thickness was taken as 5 cm.

Standard used at CAMS for samples “\*” is 07KNSTD with <sup>10</sup>Be isotope ratios = 2.85x10<sup>-12</sup>. For samples “§” standard is LLNL3000 with <sup>10</sup>Be isotope ratios = 3x10<sup>-12</sup>. KNSTD is the standard for Al samples.

Standard used at ASTER is NIST SRM4325 (=NIST\_27900) with <sup>10</sup>Be isotope ratios = 2.79x10<sup>-11</sup>, equivalent to 07KNSTD.

ext. (int.) Uncert. = external (internal) uncertainty



435

436 **Figure 10.** Depth profile (photos in Figs. S5 and S7) results using the Hidy et al. (2010)  
 437 software. Model surface ages consistent with  $^{10}\text{Be}$  and  $^{26}\text{Al}$  concentrations for T2 and T3' depth  
 438 profile samples, with or without outliers, are indicated.

439

## 440 **5 Interpretation and discussion**

### 441 **5.1 Correlation of terrace ages with climate**

442 Whether a stream can transport sediments (hence emplace fans) or incise along its channel  
443 (hence abandon terraces) is highly dependent on climate (e.g., Whipple and Tucker, 1999;  
444 Mériaux et al., 2012). Typically, during glacial periods, stream power and sediment load are  
445 limited, thus unfavorable to fan deposition. Glacier melting at the beginning of interglacials, due  
446 to warmer climate, causes rapid increase of stream power and sediment transport, which in turn  
447 promotes fill terrace aggradation and broad fan deposition. Conversely, it is well-established that  
448 at the end of the warm and humid early Holocene Climatic Optimum (HCO, ~10 to ~5 ka),  
449 coeval with lake high-stands on the Tibetan plateau (Gasse et al., 1991), a shift to drier climate  
450 led to generally renewed river incision, terrace abandonment and lake level drop throughout  
451 North-Africa, Eurasia and Tibet (e.g., Gasse et al., 1990; Avouac et al., 1996; Brown et al., 2003;  
452 Li et al., 2005; Van Der Woerd et al., 2002).

453 The four main surface age groups we obtain,  $206 \pm 25$  ka for T4,  $112 \pm 21$  ka for T3-T3' (or  
454 ~96 ka for T3 and ~113 ka for T3'),  $16 \pm 3$  ka for T2 and  $10 \pm 2$  ka for T0s, correlate well with the  
455 last four warm climatic periods at ~200 ka (MIS-7 interglacial), ~115 ka (Eemian interglacial),  
456 ~16 ka (post-Last Glacial Maximum, MIS-2, melting), and ~10 ka (Holocene interglacial) (green  
457 bands in Fig. 9). The Eemian and Holocene ages we obtain at Taersa are similar, within  
458 uncertainty, to the  $^{10}\text{Be}$  ages (~110 and 11 ka) found 18 km to the east, north of the Karakax  
459 river by Peltzer et al. (2020) (their Site 4: large fan offsets first identified by Peltzer et al., 1989).  
460 Likewise, within uncertainty, our youngest terrace ages are consistent with the OSL

461 abandonment age ( $\sim 9 \pm 1$  ka) they found  $\sim 10$  km west of Taersa (Fig. 1b) for one offset terrace  
462 ( $\sim 10$  m above present fluvial channel, their Site 1) of a southern tributary of the Karakax river.

463 The Taersa site, however, uniquely preserves the oldest ( $\sim 210$  ka) and highest ( $> 110$  m above  
464 the Karakax river) conical fan surface dated thus far along the Karakax valley, and possibly for  
465 now within the northern Tibet Plateau. Consequently, it is possibly also the only site where the  
466 largest horizontal and vertical cumulative offsets are preserved along the KXF.

467

## 468 **5.2 Fault slip rates since $\sim 210$ ka**

469 Combining alluvial surface abandonment ages and riser offsets provides bounds on slip rates  
470 over a  $\sim 210$  ka-long timescale. Matching the T4 abandonment age ( $206 \pm 25$  ka) with the total  
471 offsets of the current T4 southeastern limit and the inferred western T4 riser top ( $\sim 500 \pm 50$  and  
472  $496 \pm 24$  m, respectively) yields  $2.4(+0.4/-0.3)$  mm/yr (Figs. 3c, 7, 11a and Table 2). Combining  
473 the T4/T3' current riser base offset ( $255 \pm 10$  m) with the inferred oldest age of T3' east ( $127 \pm 8$  ka  
474 based on that on T3 west) yields a minimum rate of  $2.0(+0.2/-0.1)$  mm/yr. Taking the inferred  
475 youngest age of T3 east ( $97 \pm 6$  ka based on that on T3 west) with the current offset ( $255 \pm 5$  m) of  
476 the T3'/T3 riser base yields  $2.6 \pm 0.2$  mm/yr. Matching the offset of the current T3/T2 western  
477 riser base ( $200 \pm 20$  m) with the inferred youngest  $97 \pm 6$  ka age of T3 yields  $2.1(+0.3/-0.2)$  mm/yr  
478 (Figs. 3c, 11a, S6 and Table 2). Lastly, we take the age of the  $22.9 \pm 1.5$  m offset of the base of  
479 the T2/T0' riser (Figs. 3e, S4 and S6), that necessarily postdates the total incision (10 m) of T2  
480 (abandoned after  $16 \pm 3$  ka) by the Holocene Taersa tributary, to be  $10 \pm 2$  ka, which is consistent  
481 with a slip rate of  $2.3(+0.6/-0.4)$  mm/yr (Figs. 11a,b, S6 and Table 2). The normal throw  
482 component across the fault at Taersa may also be estimated using the vertical offsets of T4 and  
483 T3' (Fig. 5c). The  $\sim 28$  m offset of T4 implies a throw rate of  $0.14 \pm 0.2$  mm/yr, while the 12 and

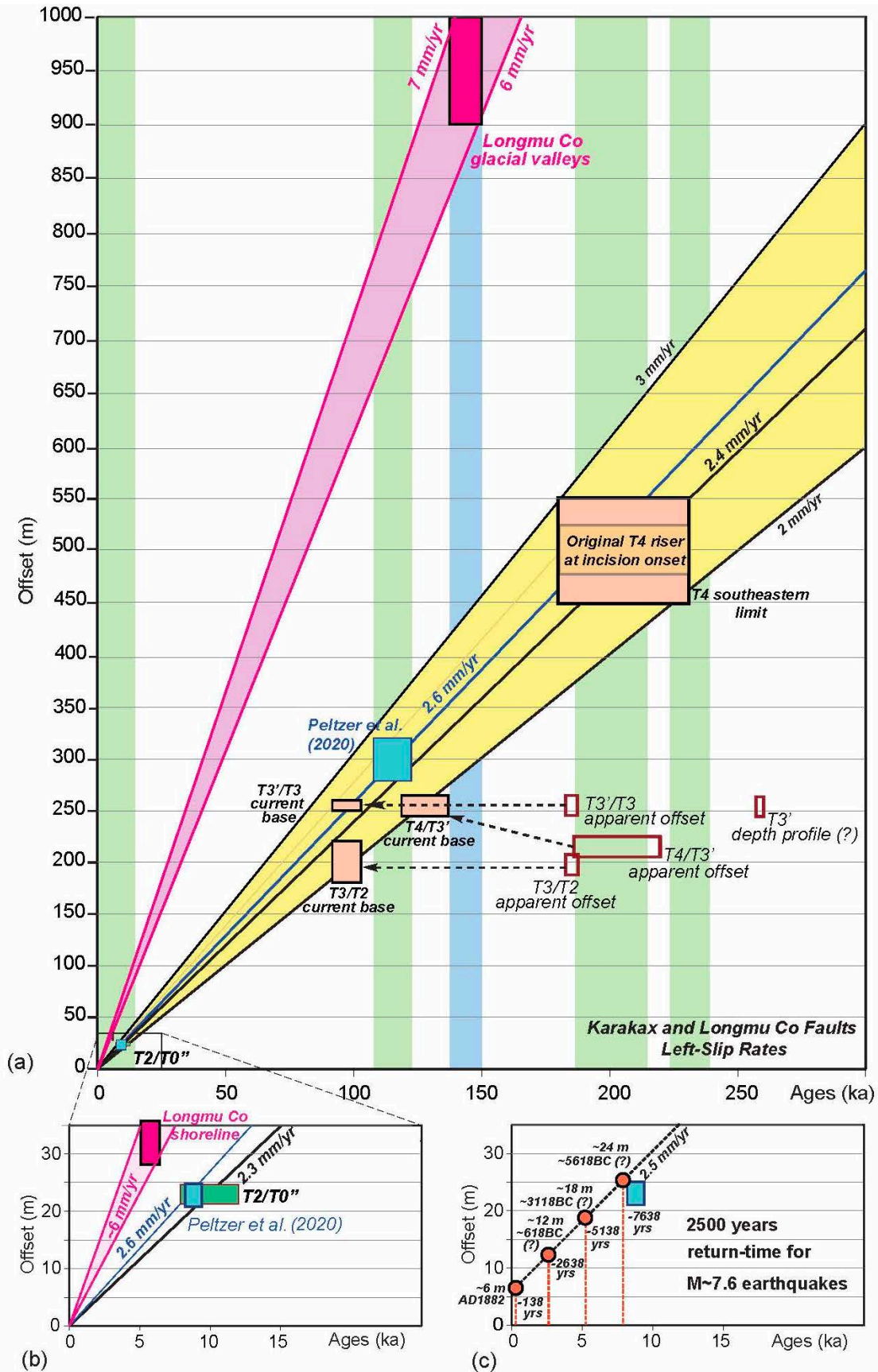
484 10 m vertical offsets of T3' and T3, respectively, are consistent with a throw rate of  $0.1 \pm 0.01$   
 485 mm/yr.

486

487 **Table 2.** Summary of offsets, ages and slip rates at Taersa.

	Offsets (m)	Ages (ka)	Slip rate (mm/yr)
T4 southeastern limit	500±50	206±25	2.4(+0.4/-0.3)
Original T4 riser at incision onset	496±24	206±25	2.4(+0.4/-0.3)
T4/T3' current base	255±10	127±8	2.0(+0.2/-0.1)
T3'/T3 current base	255±5	97±6	2.6±0.2
T3/T2 current base	200±20	97±6	2.1(+0.3/0.2)
T2/T0'' current base	22.9±1.5	10±2	2.3(+0.6/-0.4)
T0''/T0'	17.8±1.5	<10±2	2-3
T0'/T0	12.8±2.5	<10±2	2-3
T0/river bed	5.9±0.5	1882 AD	n/a

488





490 **Figure 11.** Slip rates on Karakax and Longmu Co faults. (a) Late Quaternary slip rates derived  
491 from offset/age relationships. Dashed black arrows indicate most plausible shifts of offset and  
492 ages of risers east of Taersa tributary based on T3 ages west of tributary (see text for details).  
493 Green bands are interglacial periods as in Figure 9, blue band is coldest glacial within MIS-6.  
494 See text for details. (b) Zoom on youngest terrace age range, including Peltzer et al. (2020)  
495 result. (c) Inferred large earthquakes return times consistent with simplified characteristic co-  
496 seismic slip (~6 m) and constant Holocene ~2.5 mm/yr slip rate.

497

498 Overall, the above left-lateral rates (Table 2) range between extreme values of 1.9 and 2.9  
499 mm/yr, hence a most likely long-term average between 2 and 3 mm/yr (Fig. 11a). Within ~20%  
500 uncertainty (0.4 to 0.6 mm/yr), these rates appear to have been constant over a much longer  
501 timescale (~210 ka), ~100 ka older than that documented so far. They compare well with the  
502  $2.6 \pm 0.5$  mm/yr rate recently determined by Peltzer et al. (2020) in the last ~115 ka. Locally, the  
503 total Taersa long-term rates include a vertical component (~0.1 mm/yr) that absorbs some  
504 cumulative displacement. Additionally, faulting along the southern side of the pull-apart sag  
505 within the Karakax valley (Fig. 2) may contribute to increase slightly the total Taersa slip rate.

506 Such consistent, ~2.5 mm/yr average rate values at three sites over a ~35 km-long stretch of  
507 the fault suggest that previous estimates of rates 2 to 3 times faster (6-9 mm/yr), may have been  
508 biased. Li et al.'s (2012) estimate (6-7 mm/yr) was based on just one  $^{14}\text{C}$  date (975-1020 AD) in  
509 one trench west of Taersa with no *in situ* horizontal offset measurement (Fig. 2). Gong et al.'s  
510 (2017) rate ( $7.8 \pm 1.6$  mm/yr) was derived from the OSL dating of six, reportedly fluvial, sand  
511 samples (39.7 $\pm$ 2.5 ka for T4 [their T5], 28.5 $\pm$ 1.7 ka for T3' [their T4], 21.2 $\pm$ 1.2 ka for T3 and  
512 14.5 $\pm$ 1.0 ka for T2) retrieved from the very top of unstable, south-facing risers, likely still  
513 retreating and affected by steady, long-term rejuvenation due to ongoing erosion by the Karakax  
514 river (Fig. 8a). In fact, more importantly, since the depth of these OSL samples is very shallow

515 (15-45 cm, Gong et al., 2017), and their ages much younger than those we obtain on all the  
516 relevant surfaces (Fig. 9), we suspect that the deposits they dated may include loess windblown  
517 atop the terrace surfaces much later than their fluvial abandonment ages.

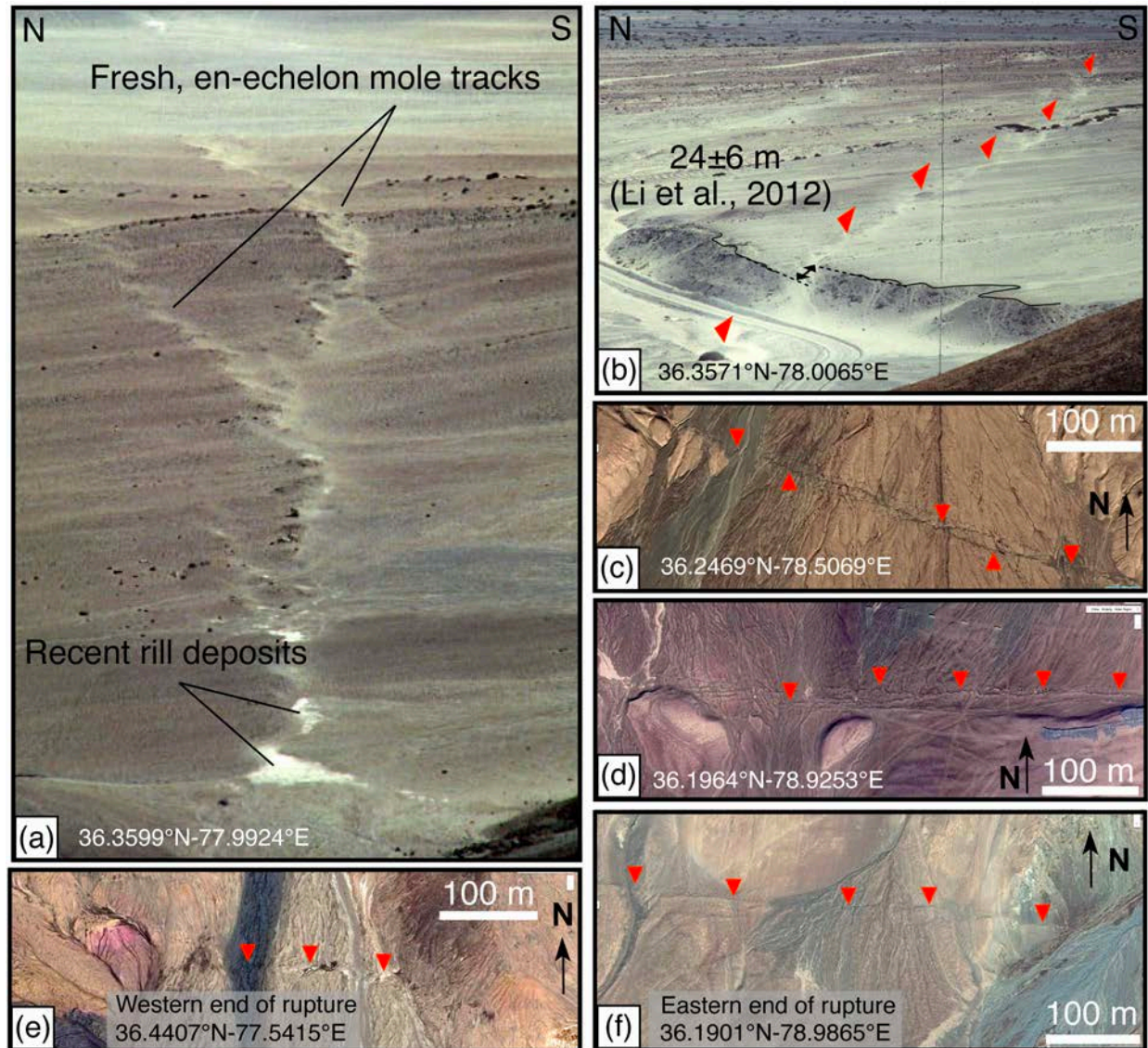
518

### 519 **5.3 Regular recurrence times of comparably large earthquakes along the** 520 **Karakax fault**

521 In the last 150 years, seven large ( $M \geq 7$ ) earthquakes have struck the broad region  
522 surrounding the West Kunlun range and western branches of the Altyn Tagh fault (ATF) (Figs. 1  
523 and 13) (SBX, 1997). The most recent ( $M_w$  6.9, 2014 and  $M_w$  7.2, 2008 Yutian earthquakes)  
524 ruptured the Ashikule left-lateral fault (Li et al., 2016) and the West Pingding normal fault (e.g.,  
525 Xu et al., 2013), within the transition zone between the ATF and the Longmu-Gozha Co fault  
526 (LGCF). Another event ( $M_s$  6.9 in 1996) ruptured a poorly studied, probably ~EW-striking fault  
527 within the Tianshuihai block, with a debated left-lateral or thrust mechanism (USGS; Ma et al.,  
528 1997). One century ago, in 1924, two events with estimated magnitudes of 7.2 and 7.5 (Chen,  
529 1988) likely ruptured segments or splays of the western ATF east of Minfeng. Even earlier on, in  
530 1882 and 1889, two large earthquakes are reported to have been strongly felt in Hotan and  
531 Yecheng, respectively (Nikonov, 1975; Ma, 1989; Avouac and Peltzer, 1993). Since little is  
532 known about these two events, however, doubts have been raised on their existence or location  
533 (Yang et al., 1991).

534 Yet, during our field work across the region, we found only one large, fresh surface rupture  
535 along faults in the West Kunlun range south of Hotan and Yecheng (Fig. 12). In the field and on  
536 high-resolution satellite images, this rupture (yellow swath in Fig. 1b) may be followed  
537 continuously for ~150 km, from ~77.5°E to 79°E. Where the fault is single-stranded, field

538 measurements imply an average left-lateral co-seismic displacement of  $6\pm 1$  m (Li et al., 2012).  
539 The facts that this rupture displays well-preserved,  $\sim 1.5$  m-high, free-faces and en-echelon mole  
540 tracks across the Sanshili and other fans (Li et al., 2012), that it affects the most recent terraces,  
541 and that it is still visible across some of the floodplains of the Karakax tributaries (Fig. 12), are in  
542 keeping with the inference that it is less than 200 years old. The measured rupture length and slip  
543 amount are consistent with a magnitude  $M7.6$  ( $M=5.08+1.16*\log[\text{surface rupture length}=150 \text{ km}]$   
544 or  $M=6.93+0.82*\log[\text{average displacement}=6 \text{ m}]$ , Wells and Coppersmith, 1994). Hence, as  
545 inferred by Avouac and Peltzer (1993), we conclude that this rupture is most likely that of the  
546 1882 Hotan earthquake (Fig. 1b).  
547



548

549 **Figure 12.** Fresh surface rupture of 1882 earthquake (see image locations in Fig. 1b). (a)  
 550 Field photograph (P. Tapponnier, 1989) of en-echelon, right-stepping scarps across fan south of  
 551 Karakax river, west of Sanshili. Note slight vertical offset north of rupture and fresh white  
 552 pluvial deposits dammed by scarp. (b) Field photograph of offset, western riser of Sanshili fan  
 553 ( $\sim 24 \pm 6$  m) and fresh surface rupture across fan surface. Note again slight vertical offset north of  
 554 fault trace. (c and d) Maxar satellite images of fresh seismic rupture across recent Karakax  
 555 tributary alluvial surfaces and active seasonal streams. (e and f) Deep open cracks close to  
 556 western and eastern terminations of  $\sim 150$  km-long, 1882 surface rupture, respectively.

557

558 Finally, the epicenters of one historical event and one recent earthquake both lie in the SW  
559 Tarim basin, just north of the West Kunlun range. The 2015, Mw 6.4 Pishan earthquake ruptured  
560 a blind, south-dipping thrust west of Hotan (Fig. 1a) (e.g., Lu et al., 2016; Wen et al., 2016;  
561 Guilbaud et al., 2017; Laborde et al., 2019). The poorly documented, possibly larger, 1889 event,  
562 tentatively located near Yecheng, might also have ruptured a blind thrust in the Kunlun foreland,  
563 south of the emergent, active Mazartagh thrust ramp (Fig. 13a).

564 The large 1882 Karakax surface break appears to be the latest in a sequence of similar  
565 ruptures with comparable amounts of co-seismic slip. Previous field measurements (Li et al.,  
566 2012) documented cumulative offset amounts of ~12, ~18 and ~24 m across four young fluvial  
567 fans along the central ~50 km of the rupture. At Taersa, our new Matlab measurements confirm  
568 values of ~6, ~13, ~18 and ~23 m across the lowermost, Holocene ( $10 \pm 2$  ka), alluvial terraces  
569 (Fig. 3e). The  $\sim 2.5 \pm 0.5$  mm/yr slip rate at this site would thus be consistent with characteristic  
570 slip (~6 m) event's return times of  $\sim 2500 \pm 500$  years (Fig. 11c). Note that such long recurrence  
571 times preclude the use of historical records to assess seismic hazard on the fault. The rare  
572 preservation of four cumulative co-seismic offsets over the entire Holocene period yields a  
573 characteristic slip record that would be hard to obtain from trenching, even where sedimentary  
574 records reach back that long (e.g., Daëron et al., 2007).

575

#### 576 **5.4 Slip-rate along the Karakax fault at the millennial timescale**

577 The ~210 ka, 2-3 mm/yr slip rate we obtain is slower than average rates estimated  
578 geodetically across the West Kunlun range during the last ~20 years: e.g.,  $7 \pm 3$  mm/yr (GPS,  
579 Shen et al., 2001),  $5 \pm 5$  mm/yr (Interferometric Synthetic Aperture Radar [InSAR], Wright et al.,

580 2004). As discussed below, this may be a corollary consequence of the complex crustal  
581 deformation and faulting geometry across the western tip of Tibet (Figs. 1 a and 13a).

582 On a long-term, geological timescale, matching the Karakax river ~80 km offset (Gaudemer  
583 et al., 1989, Ding et al., 2004) with the likely onset age ( $\geq 24$  Ma) of rapid sedimentation in the  
584 Tarim basin's Kunlun foreland and of sustained tectonic uplift along the West Kunlun range (e.g.,  
585 Matte et al., 1996; Sobel and Dumitru, 1997; Métivier et al., 1999; Cao et al., 2015), would yield  
586 a long-term slip rate of  $\leq 3.3$  mm/yr, consistent, within uncertainties, with the average late  
587 Quaternary rate we document here. The similar ~80 km offset of the neighboring Karakax and  
588 Yurungkax, two comparably large rivers crossing the KXF across nearly impassable  
589 gorges/canyons (Fig. 1a), have long been described and clearly attributed to sinistral movement  
590 along the fault (e.g., Gaudemer et al., 1989; Ding et al., 2004). The two river floodplains are, and  
591 must have long been, captive within their deeply incised passages across mountain ranges that  
592 are now 6000 to 7000 m-high. That the highest Kunlun peaks NW and SE of the offset Karakax  
593 river are ~6300 and ~6698 m-high, i.e., ~2600 m and ~3000 m above the present valley floor  
594 (~3700 m), respectively (Fig. 1b), requires that these large offsets be nearly coeval with the onset  
595 of mountain uplift.

596 The ~24 Ma, ~210 ka, ~110 ka, and ~10 ka slip rates along the Karakax splay of the ATF  
597 would thus all fall between 2 and 3.3 mm/yr, in keeping with a long (~2500 years) return time  
598 for  $M \sim 7.6$  earthquakes and a total, post-early Miocene offset of ~80 km. That relatively slow rate  
599 is surprising given the clear, continuous surface trace, the fairly large co-seismic and geological  
600 offsets, the prominent ~150 km-long 1882 surface rupture, and the exceptionally well-preserved  
601 geomorphic expression of the fault (Fig. 12). Peltzer et al. (2020) suggested that variable slip or  
602 erosion rates might account for the non-linear relationship between progressive scarp

603 degradation and cumulative displacement along the fault. Our results tend to support the latter,  
604 although complexities in the fault trace involving pull-apart sags and releasing bends, hence sub-  
605 parallel surface strands, in part hidden within the fast-evolving, modern Karakax river floodplain,  
606 likely play a significant role.

607

### 608 **5.5 Left-lateral slip rate along the Longmu Co fault**

609 While we do not provide here more local dates along the Longmu Co fault (southern branch  
610 of the LGCF) south of the Sumxi-Longmu Lakes, the offsets shown in Figure 4 ( $32\pm 4$  and  
611  $950\pm 50$  m) are newly-derived from a dedicated, small-scale UAV survey and from recent (2021)  
612 high-resolution “Maxar Technology” satellite images, respectively. Age constraints for these two  
613 different cumulative offsets may be suitably deduced from reliable, published, local and regional  
614 dating by Gasse et al. (1991), Avouac et al. (1996), and Amidon et al. (2013). The twin Sumxi  
615 and Longmu Lakes were long-connected as a unique, large lake with maximum water heights at  
616 least  $\sim 230$  m above present level (Avouac et al., 1996) during the early HCO ( $\sim 10$  to  $\sim 5$  ka,  
617 Gasse et al., 1991). The  $32\pm 4$  m left-lateral offset of the topmost shoreline of the paleo-Sumxi-  
618 Longmu Lake must post-date the abandonment of that shoreline as the lake level rapidly dropped  
619 down at the end of the HCO (6-5.5 ka, Avouac et al., 1996). This implies a slip rate on the  
620 Longmu Co fault of  $5.6\pm 0.9$  mm/yr (Fig. 11b).

621 The larger offsets ( $\sim 950\pm 50$  m) of the narrow glacial streams, now captive within the  
622 abandoned glacial valleys crossing the fault south of the lakes, likely post-date the MIS-6 glacial  
623 maximum ( $\sim 180$ - $140$  ka, Fig. 9), after which incision began, a timing in keeping with the age of  
624 the oldest, recessional frontal moraine ( $34.414^\circ\text{N}$ - $80.046^\circ\text{E}$ ) dated at  $123\pm 5$  ka by Amidon et al.  
625 (2013). Note that this moraine is located only  $\sim 21$  km southwest of the offset shoreline site (Fig.

626 4) and ~8 km due south of the westernmost abandoned shorelines of Sumxi-Longmu Lake  
627 (Avouac et al., 1996). Assuming that the glacial valley offsets post-date glacial retreat (e.g.,  
628 Chevalier et al., 2005), between ~150 and 140 ka, their  $950\pm 50$  m average sinistral offset would  
629 imply a slip rate of  $6.5\pm 0.4$  mm/yr (Fig. 11a). We conclude that the slip rate along the Longmu  
630 Co fault may be significantly faster than the value proposed by Chevalier et al. (2017) ( $< 3$  mm/yr  
631 at a site located ~15 km west of the offset shoreline above), that may have been biased by the  
632 ages of cobbles transported downstream by post-glacial reworking of upstream moraine deposits.  
633 Note that the two rate values derived here along the central Longmu Co fault south of Lake  
634 Sumxi are within the range of those inferred at various timescales by Raterman et al. (2007).

635

## 636 **5.6 Large-scale slip partitioning, triple junction kinematics and crustal** 637 **block tectonics across western Tibet**

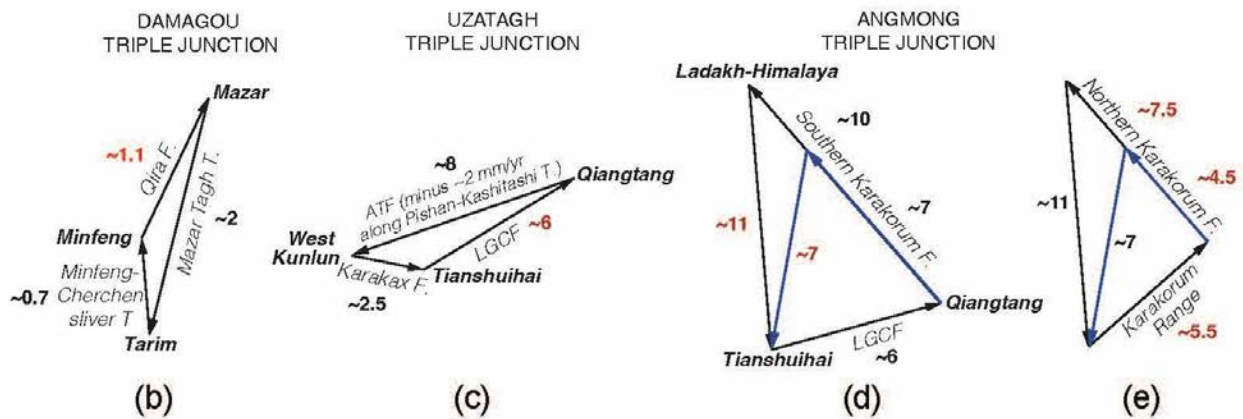
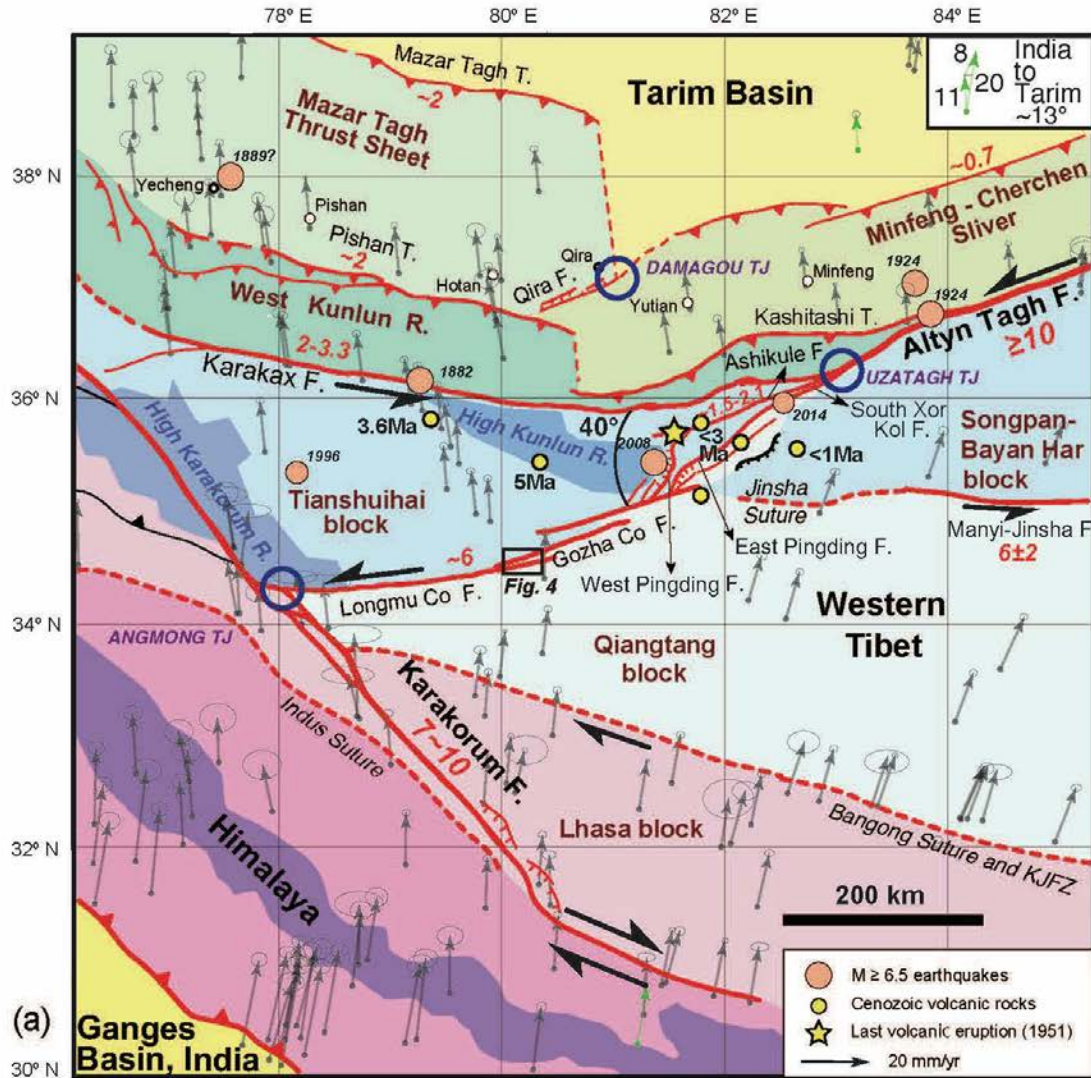
638 Earlier studies along the ATF suggested Quaternary slip rates of up to 20-30 mm/yr (e.g.,  
639 Molnar et al., 1987; Molnar and Lyon-Caen, 1989; Peltzer et al., 1989; Mériaux et al., 2004,  
640 2005; Ryerson et al., 2006), the latter three at specific field sampling sites along the central and  
641 eastern ATF. While local rates  $\geq 20$  mm/yr have been disputed, rates between ~10 and 15 mm/yr  
642 along the fault from ~84 to 93°E are now well-established over different timescales (e.g., Gold et  
643 al., 2011; Mériaux et al., 2012; Daout et al., 2018 and references therein). How rates  $\geq 10$  mm/yr  
644 on the central ATF decrease to only 2-3 mm/yr in the Karakax valley must be accounted for. The  
645 most plausible reason is the westward increasing complexity of the ATF system. While relatively  
646 linear, although segmented into parallel strands by releasing and restraining bends east of 84°E,  
647 the fault partitions westwards into distinct branches separating rising mountains from broad  
648 basins (Figs. 1 a and 13a). Whereas it is essential to assess crustal kinematics across western



649 Tibet, such splitting into splays with strike-slip, thrust or normal components remains to be  
650 accurately quantified.

651 The central ATF divides into two main faults (KXF and LGCF) at the Uzatagh triple junction  
652 (83°E, Fig. 13a). Near that junction, where the strike of the KXF starts veering northwards by  
653 ~40°, the sub-parallel Pishan-Kashitashi thrust, which raises the West Kunlun range to maximum  
654 elevations of ~6000-6700 m, also terminates. A similar ~40° clockwise turn occurs near 81°E in  
655 the Tarim foreland, between the emergent Minfeng-Cherchen sliver- and Mazar Tagh thrusts,  
656 that parallel the ATF and KXF, respectively. We thus interpret the ~NE-striking, dominantly  
657 normal, Qira fault zone (Avouac and Peltzer, 1993), to merge with both the Minfeng-Cherchen  
658 sliver thrust and a ~NS-striking ramp bounding the eastern side of the Mazar Tagh thrust sheet.  
659 Such a connection, near Qira, may be regarded as another triple junction (Damagou junction,  
660 Fig. 13a). Southwest of Uzatagh, the ATF splits into a complex pull-apart system with oblique  
661 sinistral/normal branches that merge back again southwestwards into the left-stepping LGCF  
662 (Figs. 1 a and 13a). While the M~7, 2008 and 2014 Yutian earthquakes ruptured the  
663 northwestern (West Pingding and Ashikule-Xor Kol) branches of that system, no large event has  
664 been recorded yet along the southeastern branch, although it follows a deep, active rift between  
665 the highest mountains (>6900-7100 m) of the West Kunlun range (Fig. 13a). Finally, farther SW,  
666 the Longmu Co fault merges with the southern and northern Karakorum faults at the Angmong  
667 triple junction, which also marks the southern termination of the high Karakorum range (Fig.  
668 13a), where >40 km of post-Miocene crustal heave has occurred (Van Buer et al., 2015).

669



670

671 **Figure 13.** Block tectonics model consistent with updated fault slip rates across western Tibet. (a)

672 Summary of late Quaternary slip rates (numbers in red, in mm/yr) along main active faults (F.,

673 *red lines) and thrusts (T., red lines with teeth) separating crustal blocks between India and*  
674 *Tarim (colored, after Wittlinger et al., 2004), with GPS vectors (small arrows) relative to stable*  
675 *Eurasia (Wang and Shen, 2020). Large blue circles are three main triple junctions (TJ). Dark*  
676 *blue/purple polygons highlight the highest topography along the Kunlun, Karakorum and*  
677 *Himalayan ranges (R.). Small black box along LGCF indicates location of Figure 4. (b-e)*  
678 *Triangular diagrams consistent with vector sums of late Quaternary slip rates along faults*  
679 *separating blocks around triple junctions (red numbers are predicted rates; see discussion in*  
680 *text). Top right inset is triangular diagram between current GPS vectors (green) just north of*  
681 *Himalaya and in Tarim basin.*

682

683         While few long-term slip rates are well-constrained except along the ATF-KXF and  
684 Karakorum faults, InSAR measurements now reveal  $\sim 0.7$  mm/yr of  $\sim$ NS shortening across the  
685 Minfeng-Cherchen thrust and  $6 \pm 2$  mm/yr of  $\sim$ EW sinistral motion along the western Manyi-  
686 Jinsha fault (Daout et al., 2018) (Fig. 13a). Field studies imply  $\sim$ NS shortening rates of  $\sim 2$ - $2.5$   
687 and  $\sim 1.5$ - $2.5$  mm/yr across the Pishan and Mazar Tagh thrusts, respectively (Guilbaud et al.,  
688 2017; Laborde et al., 2019). If assumed constant since shortening began in the West Kunlun  
689 range ( $\sim 24$  Ma), the sum of the latter rates ( $\sim 3.5$ - $5$  mm/yr) would be consistent with subduction  
690 of the Tarim lithospheric mantle to a depth of  $\sim 200$  km (88-125 km beneath the  $\sim 90$  km depth of  
691 the west Tibetan Moho) (Lyon-Caen and Molnar, 1984; Wittlinger et al., 2004), in classic plate  
692 tectonic behavior, coherent with young volcanism south of the West Kunlun range (small yellow  
693 circles in Fig. 13a). Lastly, along the Ashikule fault, cosmogenic dating of terrace offsets  
694 suggests rates of  $\sim 1.5$ - $2.1$  mm/yr (Pan et al., 2015) (Fig. 13a).

695         Kinematic triangular diagrams (Fig. 13b-e) fitting the vector sums of rates along the faults  
696 that separate the seven west-Tibetan blocks (Tarim, Mazar, Minfeng, Qiangtang, West Kunlun,  
697 Tianshuihai, Ladakh-Himalaya; color-coded in Fig. 13a), which appear to take up much more  
698 seismic strain than does internal deformation, clearly support block tectonics (e.g., Meyer et al.,

699 1998; Raterman et al., 2007). Specifically, at the Damagou junction, divergent thrusting on the  
700 Mazar Tagh and Minfeng thrusts results in  $\sim 1.1$  mm/yr of  $\sim$ NNE extension along the Qira fault  
701 zone (Fig. 13b). The decrease in sinistral rate between the ATF and KXF is consistent with  
702 transfer, at the Uzatagh junction, of  $\sim 6$  mm/yr of slip along the LGCF (Fig. 13c) in a direction  
703 enabling extension along the eastern boundary of the West Kunlun range. That rate is consistent  
704 with both the  $32 \pm 4$  m offset of the Sumxi-Longmu Lake topmost shoreline, abandoned  $\sim 6$ -5.5 ka  
705 ago (Gasse et al., 1991; Avouac et al., 1996) and the larger offsets ( $950 \pm 50$  m) of Eemian ( $123 \pm 5$   
706 ka, Amidon et al., 2013) glacial valleys (Fig. 4). Finally, the vector sum of rates along the  
707 southern Karakorum ( $\sim 10$  mm/yr, Chevalier et al., 2005) and LGCF ( $\sim 6$  mm/yr) predicts  $\sim 11$   
708 mm/yr of  $\sim$ NS shortening west of the Angmong junction (Fig. 13d). This may be further  
709 decomposed into  $\sim 4.5$ -7.5 mm/yr of dextral motion along the northern Karakorum fault and  $\sim 5.5$   
710 mm/yr of shortening across the high Karakorum range (Fig. 13e). Note that a faster dextral slip  
711 rate along the central Karakorum fault is consistent with very short-term InSAR geodetic  
712 observation (Wang and Wright, 2012). Most importantly, the kinematics of the latter, Angmong  
713 junction, would thus account for the rise of the second highest mountain range in Asia after the  
714 central Himalayas. The dextral rate decrease and the glaciated, high topography past that  
715 junction would explain why the active Karakorum fault was mistakenly inferred by some (e.g.,  
716 Robinson, 2009) to terminate north of  $\sim 34^\circ$ N.

717 Detailed field studies are still lacking in the region separating the Himalayas from the Tarim  
718 basin. Active faults that might bound the steep SW and NE faces of the West Kunlun and  
719 Karakorum ranges (dark blue patches in Fig. 13a), contributing to the deformation budget across  
720 the plateau, remain unexplored. This notwithstanding, however, a pattern of regional  
721 deformation dominated by block faulting seems to be inescapable. Triple junction-governed slip-

722 partitioning, similar to that long-successful in plate tectonics (e.g., McKenzie and Morgan,  
723 1969), appears to account best for changes in slip rates at the merging points between the central  
724 ATF, KXF and LGCF, southern and northern Karakorum and Longmu Co faults, and between  
725 the Qira fault, Mingfeng-Cherchen and Mazar Tagh thrusts (Fig. 13a). Likewise, the fact that the  
726 highest mountains in western Tibet abruptly terminate near two of these junctions is best  
727 explained by triple junction kinematics. Stronger crustal shortening, accounting for both the  
728 maximum elevations of the Karakorum range and northwestward right-lateral slip decrease along  
729 the eponymous fault (Chevalier et al., 2016), may just be interpreted as a simple consequence of  
730 such kinematics. While the current, local geodetic dataset remains insufficient, both space- and  
731 time-wise, to fully corroborate block tectonics, the main amplitude and directional changes of  
732 extant GPS vectors (a total of  $\sim 13^\circ$  anticlockwise, top right inset in Fig. 13a, Wang and Shen,  
733 2020) between the Himalaya and the Tarim tend to coincide with the positions of the main active  
734 faults. That several of the largest faults follow ancient, likely weak, crustal/lithospheric divides  
735 between the main terranes of the Tibetan collage (e.g., Oytog, Jinsha and Bangong sutures, Matte  
736 et al., 1996; Wittlinger et al., 2004), mechanically justifies the observed behavior. Crucially,  
737 while complex, the late Quaternary kinematics across western Tibet strongly support simple  
738 block tectonics rather than broadly diffuse deformation (Peltzer and Tapponnier, 1988; Meyer et  
739 al., 1998; Tapponnier et al., 2001; Loveless and Meade, 2011).

740

## 741 **6 Conclusion**

742 New slip rate measurements along the Karakax and Longmu Co faults, westernmost  
743 branches of the Altyn Tagh fault, help understand broad-scale block kinematics across the  
744 western tip of the Tibetan Plateau, between the Ganges plain and the Tarim basin. Over the last

745 ~210 ka (age of the oldest alluvial surface dated thus far in northwestern Tibet), and possibly  
746 since ~24 Ma, the slip rate along the Karakax fault seems to have remained constant, between 2  
747 and 3 mm/yr, as recently shown by Peltzer et al. (2020) since ~115 ka. Since the beginning of the  
748 Holocene, great earthquakes ( $M \sim 7.6$ ) appear to have ruptured at least ~150 km of the fault with  
749 fairly regular, if long ( $\sim 2500 \pm 500$  years) return times, and with characteristic co-seismic slip  
750 amounts on order of 6 m - as was the case for the last, likely 1882 AD event - for four such  
751 events. These conclusions are based on the combination of high-resolution digital elevation  
752 surveys and dating of alluvial fan and terrace offsets at Taersa in the Karakax valley, and of lake  
753 shoreline and glacial valley offsets by the Longmu Co fault south of Sumxi Lake. Along the  
754 Karakax fault, the well-known, ~80 km offset of the Karakax river may have accrued since uplift  
755 of the West Kunlun range started in the early Miocene (~24 Ma). The sum of the slip rates on the  
756 Longmu Co fault (~6 mm/yr) with those on the Karakax fault (~2-3 mm/yr) and on the active  
757 thrusts ( $2 \times \sim 2$  mm/yr =  $\sim 4$  mm/yr) along the Tarim foreland of the Kunlun, yields a total of  $\geq 12$   
758 mm/yr along the central Altyn Tagh fault, between central Tibet and the Tarim, in keeping with  
759 the modern InSAR rate ( $\geq 10.5$  mm/yr) obtained by Daout et al. (2018). To a first order, at the  
760 scale of the entire western plateau, block tectonics and triple junction kinematics appear to  
761 account for the recent and late Tertiary continental deformation, even though the seven blocks  
762 involved, particularly the Tianshuihai block, may not be torsionally rigid. Specifically, the  
763 junction between the conjugate Longmu Co and Karakorum strike-slip faults may be key to  
764 explain the rise and abrupt southern termination of the high Karakorum range, second highest in  
765 the world. Our results bridge the gaps between present and long-term geological history, and  
766 between broad-scale geodesy and local field evidence.  
767

768 **Acknowledgments and Data**

769 This work was supported by the 2nd Tibetan Plateau Scientific Expedition of the Ministry of  
770 Science and Technology of China (2019QZKK0901), the National Natural Science Foundation  
771 of China (41672211, 41941016), the China Geological Survey (DD20190059), the Basic  
772 Research Funds of the Institute of Geology, Chinese Academy of Geological Sciences  
773 (JYYWF201810), and Key Special Project for Introduced Talents Team of Southern Marine  
774 Science and Engineering Guangdong Laboratory (Guangzhou) (GML2019ZD0201). The first  
775 exploratory 1989 field trip was funded by INSU-CNRS, the French Ministry of Research and  
776 Higher Education and the Chinese Academy of Geological Sciences (CAGS). The 1995 field  
777 work was supported by a NASA SIC-C investigation. LLNL's participation in the 1995 sampling  
778 trip as well as cosmogenic dating of those 1995 samples were supported by the Laboratory  
779 Directed Research Project (01-ERI-009) at Lawrence Livermore National Laboratory operating  
780 under the auspices of the US Department of Energy by Lawrence Livermore National Laboratory  
781 under Contract DE-AC52-07NA27344. Dating at the ASTER AMS French national facility  
782 (CEREGE, Aix-en-Provence) was supported by the INSU-CNRS, the French Ministry of  
783 Research and Higher Education, IRD, and CEA. We thank J.P. Avouac for his participation in  
784 the 1989 field expedition, and M. Bai for his help with the LiDAR processing and Matlab run.  
785 We thank the Editor, Associate Editor, and two anonymous reviewers for their constructive  
786 comments. Ages and digital elevation surveys (LiDAR and UAV) data are available at  
787 [https://zenodo.org/record/5115549#.YPjRpC0RjA\\_](https://zenodo.org/record/5115549#.YPjRpC0RjA_)

788

789 **References**

- 790 Amidon, W. H., Bookhagen, B., Avouac, J. P., Smith, T., & Rood, D. (2013), Late Pleistocene  
791 glacial advances in the western Tibet interior. *Earth and Planetary Science Letters*, 381, 210-  
792 221. <https://doi.org/10.1016/j.epsl.2013.08.041>.
- 793 Armijo, R., Tapponnier, P., & Han, T. (1989), Late Cenozoic right-lateral strike-slip faulting in  
794 southern Tibet. *Journal of Geophysical Research Solid Earth*, 94(B3), 2787-2838.  
795 <https://doi.org/10.1029/JB094iB03p02787>.
- 796 Avouac, J. P., & Peltzer, G. (1993), Active tectonics in southern Xinjiang, China: Analysis of  
797 terrace riser and normal fault scarp degradation along the Hotan-Qira fault system. *Journal of*  
798 *Geophysical Research Solid Earth*, 98(B12), 773-807. <https://doi.org/10.1029/93JB02172>.
- 799 Avouac, J. P., & Tapponnier, P. (1993), Kinematic model of active deformation in central Asia.  
800 *Geophysical Research Letters*, 20(10), 895–898. <https://doi.org/10.1029/93GL00128>.
- 801 Avouac, J. P., Dobremez, J. F., & Bourjot, L. (1996), Palaeoclimatic interpretation of a  
802 topographic profile across middle Holocene regressive shorelines of Longmu Co (Western  
803 Tibet). *Palaeogeography Palaeoclimatology Palaeoecology*, 120, 93-104.  
804 [https://doi.org/10.1016/0031-0182\(96\)88700-1](https://doi.org/10.1016/0031-0182(96)88700-1).
- 805 Balco, G., Stone, J. O., Lifton, N. A., & Dunai, T. J. (2008), A complete and easily accessible  
806 means of calculating surface exposure ages or erosion rates from  $^{10}\text{Be}$  and  $^{26}\text{Al}$   
807 measurements. *Quaternary Geochronology*, 3(3), 174-195.  
808 Doi:10.1016/j.quageo.2007.12.001.
- 809 Bevington, P.R., & Robinson, D.K. (2002), Data Reduction and Error Analysis for the  
810 Physical Sciences, 336 pp., McGraw-Hill, New York.
- 811 Blisniuk, P. M., & Sharp, W. D. (2003). Rates of late Quaternary normal faulting in central Tibet from  
812 U-series dating of pedogenic carbonate in displaced fluvial gravel deposits. *Earth and Planetary*  
813 *Science Letters*, 215(1–2), 169–186.



- 814 Brown, E. T., Bendick, R., Bourlès, D. L., Gaur, V., & Yiou, F. (2003), Early Holocene climate recorded  
815 in geomorphological features in Western Tibet. *Palaeogeography Palaeoclimatology*  
816 *Palaeoecology*, 199(1), 141-151. [https://doi.org/10.1016/S0031-0182\(03\)00501-7](https://doi.org/10.1016/S0031-0182(03)00501-7).
- 817 Cao, K., Wang, G. C., Bernet, M., van der Beek, P., & Zhang, K. X. (2015), Exhumation history  
818 of the West Kunlun Mountains, northwestern Tibet: Evidence for a long-lived, rejuvenated  
819 orogen. *Earth and Planetary Science Letters*, 432, 391-403. Doi:10.1016/j.epsl.2015.10.033.
- 820 Chen, X. (1988), Xinjiang earthquake catalogue ( $m_s \geq 4.7$ ) from 1600 to 1987. *Inland*  
821 *Earthquakes*, 3, 320-340. <https://doi:10.16256/j.issn.1001-8956.1988.03.016>
- 822 Chevalier, M. L., Ryerson, F. J., Tapponnier, P., Finkel, R. C., Van der Woerd, J., Li, H., & Liu,  
823 Q. (2005), Slip-rate measurements on the Karakorum Fault may imply secular variations in  
824 fault motion. *Science*, 307(5708), 411-414. <https://doi:10.1126/science.1105466>.
- 825 Chevalier, M. L., Van der Woerd, J., Tapponnier, P., Li, H., Ryerson, F. J., & Finkel, R. C.  
826 (2016), Late Quaternary slip-rate along the central Bangong-Chaxikang segment of the  
827 Karakorum fault, western Tibet. *Geological Society of America Bulletin*, 128(1-2), 284-314.  
828 <https://doi:10.1130/b31269.1>.
- 829 Chevalier, M. L., Pan, J., Li, H., Sun, Z., Liu, D., Pei, J., et al. (2017). First tectonic-  
830 geomorphology study along the Longmu-Gozha Co fault system, Western Tibet. *Gondwana*  
831 *Research*, 41, 411-424. <https://doi:10.1016/j.gr.2015.03.008>.
- 832 Cowgill, E. (2007), Impact of riser reconstructions on estimation of secular variation in rates of  
833 strike-slip faulting: Revisiting the Cherchen River site along the Altyn Tagh Fault, NW  
834 China. *Earth and Planetary Science Letters*, 254(3-4), 239-255.  
835 doi:10.1016/j.epsl.2006.09.015.

- 836 Daëron, M., Klinger, Y., Tapponnier, P., Elias, A., Jacques, E., & Sursock, A. (2007), 12,000-  
837 year-long record of 10 to 13 paleoearthquakes on the Yammouneh fault, Levant fault system,  
838 Lebanon. *Bulletin of the Seismological Society of America*, 97(3), 749-771.  
839 <https://doi:10.1785/0120060106>.
- 840 Daout, S., Doin, M. P., Peltzer, G., Lasserre, C., Socquet, A., Volat, M., & Sudhaus, H. (2018),  
841 Strain partitioning and present-day fault kinematics in NW Tibet from Envisat SAR  
842 interferometry. *Journal of Geophysical Research*, 123(3), 2462-2483.  
843 <https://doi:10.1002/2017jb015020>.
- 844 DeMets, C., Gordon, R. G., Argus, D., & Stein, S. (1990), Current plate motions. *Geophysical*  
845 *journal international*, 101(2), 425-478. <https://doi.org/10.1111/j.1365-246X.1990.tb06579.x>.
- 846 Ding, G., Chen, J., Tian, Q., Shen, X., Xing, C., & Wei, K. (2004), Active faults and magnitudes  
847 of left-lateral displacement along the northern margin of the Tibetan Plateau. *Tectonophysics*,  
848 380(3-4), 243-260. Doi:10.1016/j.tecto.2003.09.022.
- 849 Farr, T., & Chadwick, O. (1996). Geomorphic processes and remote sensing signatures of  
850 alluvial fans in the Kunlun Mountains, China. *Journal of Geophysical Research*,  
851 101(E10), 23,091-23,100.
- 852 Gasse, F., T  het, R., Durand, A., Gibert, E., & Fontes, J. C. (1990), The arid–humid transition in  
853 the Sahara and the Sahel during the last deglaciation. *Nature*, 346(6280), 141-146.
- 854 Gasse, F., Arnold, M., Fontes, J. C., Fort, M., Gibert, E., Huc, A. et al. (1991), A 13,000-year  
855 climate record from western Tibet. *Nature*, 353(6346), 742-745. [https://doi:](https://doi:10.1016/j.tecto.2003.09.022)  
856 [10.1016/j.tecto.2003.09.022](https://doi:10.1016/j.tecto.2003.09.022).
- 857 Gaudemer, Y., Tapponnier, P., & Turcotte, D. (1989), River offsets across active strike-slip  
858 faults. *Annales Tectonicae*, 3, 55–76.

- 859 Gold, R. D., Cowgill, E., Arrowsmith, R., Gosse, J., Chen, X., & Wang, X. (2009). Riser  
860 diachroneity, lateral erosion, and uncertainty in rates of strike-slip faulting: A case  
861 study from Tuzidun along the Altyn Tagh Fault, NW China. *Journal of Geophysical*  
862 *Research*, 114(B04401), 1–24. <https://doi.org/10.1029/2008JB005913>
- 863 Gold, R. D., Cowgill, E., Arrowsmith, J. R., Chen, X., Sharp, W. D., Cooper, K. M., & Wang, X.  
864 (2011), Faulted terrace risers place new constraints on the late Quaternary slip rate for the  
865 central Altyn Tagh fault, northwest Tibet. *Geological Society of America Bulletin*, 123(5-6),  
866 958-978. <https://doi.org/10.1130/B30207.1>.
- 867 Gong, Z., Sun, J., Zhang, Z., Fu, B., & Jia, Y. (2017), Optical dating of an offset river terrace  
868 sequence across the Karakax fault and its implication for the late Quaternary left-lateral slip  
869 rate. *Journal of Asian Earth Sciences*, 147, 415-423.  
870 <https://doi.org/10.1016/j.jseaes.2017.07.013>.
- 871 Guilbaud, C., Simoes, M., Barrier, L., Laborde, A., Van der Woerd, J., Li, H. et al. (2017),  
872 Kinematics of active deformation across the Western Kunlun mountain range (Xinjiang,  
873 China) and potential seismic hazards within the southern Tarim Basin. *Journal of*  
874 *Geophysical Research*, 122(12), 10,398-426. Doi:10.1002/2017JB014069.
- 875 Hetzel, R., Niedermann, S., Tao, M.X., Kubik, P.W., Ivy-Ochs, S., Gao, B., Strecker, M.R.,  
876 (2002), Low slip rates and long-term preservation of geomorphic features in Central  
877 Asia. *Nature*, 417, 428–432.
- 878 Hidy, A. J., Gosse, J. C., Pederson, J. L., Mattern, J. P., & Finkel, R. C. (2010), A geologically  
879 constrained Monte Carlo approach to modeling exposure ages from profiles of cosmogenic  
880 nuclides: An example from Lees Ferry, Arizona. *Geochemistry, Geophysics, Geosystems*,  
881 11(9), 1-18. <https://doi.org/10.1029/2010gc003084>.

- 882 Kohl, C. P., & Nishiizumi, K. (1992), Chemical isolation of quartz for measurement of in-situ  
883 produced cosmogenic nuclides. *Geochimica et Cosmochimica Acta*, 56(9), 3583-3587.  
884 [https://doi.org/10.1016/0016-7037\(92\)90401-4](https://doi.org/10.1016/0016-7037(92)90401-4).
- 885 Laborde, A., Barrier, L., Simoes, M., Li, H., Coudroy, T., Van der Woerd, J., & Tapponnier, P.  
886 (2019), Cenozoic deformation of the Tarim Basin and surrounding ranges (Xinjiang, China):  
887 A regional overview. *Earth Science Reviews*, 197, 102891.  
888 <https://doi:10.1016/j.earscirev.2019.102891>.
- 889 Lal, D. (1991), Cosmic ray labeling of erosion surfaces: in situ nuclide production rates and  
890 erosion models. *Earth and Planetary Science Letters*, 104(2-4), 424-439.  
891 [https://doi:10.1016/0012-821x\(91\)90220-c](https://doi:10.1016/0012-821x(91)90220-c).
- 892 Li, H., Van Der Woerd, J., Tapponnier, P., Yann, K., Qi, X., Yang, J., & Zhu, Y. (2005), Slip  
893 rate on the Kunlun fault at Hongshui Gou, and recurrence time of great events comparable to  
894 the 14/11/2001, Mw7.9 Kokoxili earthquake. *Earth and Planetary Science Letters*, 237(1-2),  
895 285-299. <https://doi.org/10.1016/j.epsl.2005.05.041>.
- 896 Li, H., Van Der Woerd, J., Sun, Z., Si, J., Tapponnier, P., Pan, J. et al. (2012), Co-seismic and  
897 cumulative offsets of the recent earthquakes along the Karakax left-lateral strike-slip fault in  
898 western Tibet. *Gondwana Research*, 21(1), 64-87. <https://doi:10.1016/j.gr.2011.07.025>.
- 899 Li, H., Pan, J., Lin, A., Sun, Z., Liu, D., Zhang, J. et al. (2016), Coseismic Surface Ruptures  
900 Associated with the 2014Mw 6.9 Yutian Earthquake on the Altyn Tagh Fault, Tibetan  
901 Plateau. *Bulletin of the Seismological Society of America*, 106, 595–608.  
902 <https://doi:10.1785/0120150136>.

- 903 Lifton, N., Sato, T., & Dunai, T. J. (2014), Scaling in situ cosmogenic nuclide production rates  
904 using analytical approximations to atmospheric cosmic-ray fluxes. *Earth and Planetary  
905 Science Letters*, 386, 149-160. <https://doi:10.1016/j.epsl.2013.10.052>.
- 906 Lisiecki, L. E., & Raymo, M. E. (2005), A Pliocene–Pleistocene stack of 57 globally distributed  
907 benthic  $\delta^{18}\text{O}$  records. *Paleoceanography*, 20(1), 1-17. <https://doi:10.1029/2004pa001071>.
- 908 Liu, Q. (1993), Paleoclimat et contraintes chronologiques sur les mouvements récents dans  
909 l'Ouest du Tibet: failles du Karakorum et de Longmu Co-Gozha Co, lacs en pull-apart de  
910 Longmu Co et de Sumxi Co, (Doctoral dissertation). Université de Paris VII.
- 911 Loveless, J. P., & Meade, B. J. (2011), Partitioning of localized and diffuse deformation in the  
912 Tibetan Plateau from joint inversions of geologic and geodetic observations. *Earth and  
913 Planetary Science Letters*, 303(1-2), 11-24. <https://doi:10.1016/j.epsl.2010.12.014>.
- 914 Lu, R., Xu, X., He, D., Liu, B., Tan, X., & Wang, X. (2016), Coseismic and blind fault of the  
915 2015 Pishan Mw 6.5 earthquake: Implications for the sedimentary–tectonic framework of  
916 the western Kunlun Mountains, northern Tibetan Plateau. *Tectonics*, 35(4), 956-964.  
917 <https://doi:10.1002/2015tc004053>.
- 918 Lyon–Caen, H., & Molnar, P. (1984), Gravity anomalies and the structure of western Tibet and  
919 the southern Tarim Basin. *Geophysical Research Letters*, 11(12), 1251-1254.  
920 <https://doi.org/10.1029/GL011i012p01251>.
- 921 Ma, X. (Eds.) (1989), Seismotectonic map of xinjiang, lithospheric dynamics atlas of china.  
922 *China cartographic publishing house*.
- 923 Ma, S., Yao, Z., & Ji, C. (1997), The Focal Mechanism Solution for March 19, 1996  $M_s$  6.9  
924 Earthquake in XinJiang Jia-Shi Region and Related Problems. *Acta Geophysica Sinica*, 40,  
925 789-800.

- 926 Matte, P., Tapponnier, P., Arnaud, N., Bourjot, L., Avouac, J., Vidal, P. et al. (1996), Tectonics  
927 of Western Tibet, between the Tarim and the Indus. *Earth and Planetary Science Letters*,  
928 142(3-4), 311-330. [https://doi:10.1016/0012821x\(96\)00086-6](https://doi.org/10.1016/0012821x(96)00086-6).
- 929 McKenzie, D.P., & Morgan, W.J. (1969), Evolution of triple junctions. *Nature*, 224, 125–133,  
930 [doi:10.1038/224125a0](https://doi.org/10.1038/224125a0).
- 931 Mériaux, A. S., Ryerson, F., Tapponnier, P., Van der Woerd, J., Finkel, R., Xu, X., Xu, Z., &  
932 Caffee, M. (2004), Rapid slip along the central Altyn Tagh Fault: morphochronologic  
933 evidence from Cherchen He and Sulamu Tagh. *Journal of Geophysical Research*, 109(B6),  
934 1-23. [Doi:10.1029/2003jb002558](https://doi.org/10.1029/2003jb002558).
- 935 Mériaux, A. S., Tapponnier, P., Ryerson, F. J., Xu, X., King, G., van der Woerd, J., et al. (2005).  
936 The Aksay segment of the northern Altyn Tagh fault: Tectonic geomorphology,  
937 landscape evolution, and Holocene slip rate. *Journal of Geophysical Research*, 110,  
938 B04404. <https://doi.org/10.1029/2004JB003210>
- 939 Mériaux, A. S., Van der Woerd, J., Tapponnier, P., Ryerson, F., Finkel, R., Lasserre, C., & Xu,  
940 X. (2012), The Pingding segment of the Altyn Tagh Fault (91° E): Holocene slip rate  
941 determination from cosmogenic radionuclide dating of offset fluvial terraces. *Journal of*  
942 *Geophysical Research*, 117(B9). [https://doi:10.1029/2012jb009289](https://doi.org/10.1029/2012jb009289).
- 943 Métivier, F., Gaudemer, Y., Tapponnier, P., & Klein, M. (1999), Mass accumulation rates in  
944 Asia during the Cenozoic. *Geophysical Journal International*, 137(2), 280-318.  
945 <https://doi.org/10.1046/j.1365-246X.1999.00802.x>.
- 946 Meyer, B., Tapponnier, P., Gaudemer, Y., Peltzer, G., Guo, S. & Chen, Z. (1996), Rate of left-  
947 lateral movement along the easternmost segment of the Altyn Tagh fault, east of 96°E  
948 (China). *Geophysical Journal International*, 124, 29-44.

- 949 Meyer, B., Tapponnier, P., Bourjot, L., Metivier, F., Gaudemer, Y., Peltzer, G. et al. (1998),  
950 Crustal thickening in Gansu-Qinghai, lithospheric mantle subduction, and oblique, strike-slip  
951 controlled growth of the Tibet plateau. *Geophysical Journal International*, 135(1), 1-47.  
952 <https://doi.org/10.1046/j.1365-246X.1998.00567.x>.
- 953 Molnar, P., & Lyon-Caen, H. (1989), Fault plane solutions of earthquakes and active tectonics of  
954 the Tibetan Plateau and its margins. *Geophysical Journal International*, 99(1), 123-153.  
955 <https://doi.org/10.1111/j.1365-246X.1989.tb02020.x>.
- 956 Molnar, P., Burchfiel, B. C., Liang, K., & Zhao, Z. (1987), Geomorphic evidence for active  
957 faulting in the Altyn Tagh and northern Tibet and qualitative estimates of its contribution to  
958 the convergence of India and Eurasia. *Geology*, 15(3), 249-253.  
959 [https://doi.org/10.1130/0091-7613\(1987\)15](https://doi.org/10.1130/0091-7613(1987)15).
- 960 Nikonov, A. A. (1975), Migration of strong earthquakes along the greatest zones of faults in  
961 Central Asia. *Doklady Akademii Nauk*, 225(2), 306–309.
- 962 Pan, J., Li, H., Van Der Woerd, J., Sun, Z., Si, J., Pei, J. et al. (2015), The first quantitative slip-  
963 rate estimated along the Ashikule Fault at the western segment of the Altyn Tagh Fault  
964 System. *Acta Geologica Sinica (English Edition)*, 89(6), 2088-2089.  
965 <https://doi:10.1111/1755-6724.12621>.
- 966 Peltzer, G., & Tapponnier, P. (1988), Formation and evolution of strike-slip faults, rifts, and  
967 basins during the India-Asia collision; an experimental approach. *Journal of Geophysical*  
968 *Research*, 93, 15,085–15,117.
- 969 Peltzer, G., Tapponnier, P., & Armijo, R. (1989), Magnitude of Late Quaternary Left-Lateral  
970 Displacements Along the North Edge of Tibet. *Science*, 246(4935), 1285-1289.  
971 <https://doi:10.1126/science.246.4935.1285>.

- 972 Peltzer, G., Brown, N. D., Mériaux, A. S., van der Woerd, J., Rhodes, E. J., Finkel, R. C. et al.  
973 (2020), Stable rate of slip along the Karakax Section of the Altyn Tagh Fault from  
974 observation of interglacial and postglacial offset morphology and surface dating. *Journal of*  
975 *Geophysical Research: Solid Earth*, 125(5). <https://doi:10.1029/2019jb018893>.
- 976 Raterman, N. S., Cowgill, E., & Lin, D. (2007), Variable structural style along the Karakoram  
977 fault explained using triple-junction analysis of intersecting faults. *Geosphere*, 3(2), 71-85.  
978 <https://doi:10.1130/ges00067.1>.
- 979 Robinson, A. C. (2009), Evidence against Quaternary slip on the northern Karakorum Fault  
980 suggests kinematic reorganization at the western end of the Himalayan–Tibetan orogen.  
981 *Earth and Planetary Science Letters*, 286(1-2), 158-170.  
982 <https://doi:10.1016/j.epsl.2009.06.025>.
- 983 Ryerson, F., Peltzer, G., Tapponnier, P., Finkel, R., Mériaux, A., Van der Woerd, J., & Caffee,  
984 M. (1999), Active slip-rates on the Altyn Tagh Fault–Karakax Valley segment: Constraints  
985 from surface exposure dating. *Eos Trans. AGU*, 80(46), 1008.
- 986 Ryerson, F.J., Tapponnier, P., Finkel, R.C., Mériaux, A.S., Van der Woerd, J., Lasserre, C.,  
987 Chevalier, M.L., Xiwei, X., Li, H., & King, G.C.P. (2006), Applications of  
988 morphochronology to the active tectonics of Tibet, in Siame, L.L., Bourles, D.L., and  
989 Brown, E.T. ,eds., Application of Cosmogenic Nuclides to the Study of Earth Surface  
990 Processes: The Practice and the Potential. *Geological Society of America Special Paper*  
991 415, 61–86, doi: 10.1130/2006.2415(05)
- 992 Seismological bureau of Xinjiang Uygur autonomous region (1997), Instruction of Xinjiang  
993 Uygur autonomous region seismotectonic map (1:2000000), Xinjiang.



- 994 Shen, Z. K., Wang, M., Li, Y., Jackson, D. D., Yin, A., Dong, D., & Fang, P. (2001), Crustal  
995 deformation along the Altyn Tagh fault system, western China, from GPS. *Journal of*  
996 *Geophysical Research: Solid Earth*, 106(B12), 30607-30621.  
997 <https://doi:10.1029/2001jb000349>.
- 998 Sobel, E. R., & Dumitru, T. A. (1997), Thrusting and exhumation around the margins of the  
999 western Tarim basin during the India-Asia collision. *Journal of Geophysical Research*,  
1000 102(B3), 5043-5063. <https://doi.org/10.1029/96JB03267>.
- 1001 Stewart, N., Gaudemer, Y., Manighetti, I., Serreau, L., Vincendeau, A., Dominguez, S., ...  
1002 Malavieille, J. (2018), “3D\_Fault\_Offsets,” a Matlab code to automatically measure  
1003 lateral and vertical fault offsets in topographic data: Application to San Andreas, Owens  
1004 Valley, and Hope faults. *Journal of Geophysical Research*, 123, 815–835.  
1005 <https://doi.org/10.1002/2017JB014863>
- 1006 Stone, J.O. (2000), Air pressure and cosmogenic isotope production. *Journal of Geophysical*  
1007 *Research*, 105(B10), 23753-23759. <https://doi:10.1029/2000jb900181>.
- 1008 Tao, Y., Xiong, J., Zhang, H., Chang, H., & Li, L. (2020), Climate-driven formation of fluvial  
1009 terraces across the Tibetan Plateau since 200 kya: A review. *Quaternary Science Reviews*, 237,  
1010 106303. doi: 10.1016/j.quascirev.2020.106303.
- 1011 Tapponnier, P., & Molnar, P. (1977), Active faulting and tectonics in China. *Journal of*  
1012 *Geophysical Research*, 82(20), 2905-2930. <https://doi:10.1029/jb082i020p02905>.
- 1013 Tapponnier, P., Xu, Z., Roger, F., Meyer, B., Arnaud, N., Wittlinger, G., & Yang, J. (2001),  
1014 Oblique stepwise rise and growth of the Tibet Plateau. *Science*, 294(5547), 1671-1677.  
1015 <https://doi:10.1126.science.105978>.

- 1016 Van Buer, N. J., Jagoutz, O., Upadhyay, R., & Guillong, M. (2015), Mid-crustal detachment  
1017 beneath western Tibet exhumed where conjugate Karakoram and Longmu–Gozha Co faults  
1018 intersect. *Earth and Planetary Science Letters*, *413*, 144-157.  
1019 <https://doi:10.1016/j.epsl.2014.12.053>.
- 1020 Van Der Woerd, J. V., Tapponnier, P., J. Ryerson, F., Mériaux, A.-S., Meyer, B., Gaudemer, Y.,  
1021 Finkel, R. C., Caffee, M. W., Guoguan, Z., & Zhiqin, X. (2002), Uniform postglacial slip-  
1022 rate along the central 600 km of the Kunlun Fault (Tibet), from <sup>26</sup>Al, <sup>10</sup>Be, and <sup>14</sup>C dating  
1023 of riser offsets, and climatic origin of the regional morphology. *Geophysical Journal*  
1024 *International*, *148*(3), 356-388. <https://doi:10.1046/j.1365-246x.2002.01556.x>.
- 1025 Wang, H., & Wright, T. (2012), Satellite geodetic imaging reveals internal deformation of  
1026 western Tibet. *Geophysical Research Letters*, *39*(7). <https://doi:10.1029/2012gl051222>.
- 1027 Wang, M., & Shen, Z. K. (2020), Present-day crustal deformation of continental China derived  
1028 from GPS and its tectonic implications. *Journal of Geophysical Research*, *125*(2),  
1029 e2019JB018774. <https://doi:10.1029/2012gl051222>.
- 1030 Wells, D. L., & Coppersmith, K. J. (1994), New empirical relationships among magnitude,  
1031 rupture length, rupture width, rupture area, and surface displacement. *Bulletin of the*  
1032 *seismological Society of America*, *84*(4), 974-1002.
- 1033 Wen, Y., Xu, C., Liu, Y., & Jiang, G. (2016), Deformation and source parameters of the 2015  
1034 Mw 6.5 earthquake in Pishan, western China, from Sentinel-1A and ALOS-2 data. *Remote*  
1035 *sensing*, *8*(2), 134. <https://doi:10.3390/rs8020134>.
- 1036 Whipple, K. X., & Tucker, G. E. (1999), Dynamics of the stream-power river incision model:  
1037 Implications for height limits of mountain ranges, landscape response timescales, and

- 1038 research needs. *Journal of Geophysical Research*, 104(B8), 17661-17674.  
1039 <https://doi:10.1029/1999jb900120>.
- 1040 Wittlinger, G., Vergne, J., Tapponnier, P., Farra, V., Poupinet, G., Jiang, M., Su, H., Herquel, G.,  
1041 & Paul, A. (2004), Teleseismic imaging of subducting lithosphere and Moho offsets beneath  
1042 western Tibet. *Earth and Planetary Science Letters*, 221(1-4), 117-130.
- 1043 Wright, T. J., Parsons, B., England, P. C., & Fielding, E. J. (2004), InSAR observations of low  
1044 slip rates on the major faults of western Tibet. *Science*, 305(5681), 236-239.  
1045 <https://doi:10.1126/science.1096388>.
- 1046 Xu, X., Tan, X., Yu, G., Wu, G., Fang, W., Chen, J. et al. (2013), Normal-and oblique-slip of the  
1047 2008 Yutian earthquake: evidence for eastward block motion, northern Tibetan Plateau.  
1048 *Tectonophysics*, 584, 152-165. <https://doi:10.1016/j.tecto.2012.08.007>.
- 1049 Yao, T., Jiao, K., Tian, L., Yang, Z., Shi, W., & Thompson, L.G. (1996), Climatic variations  
1050 since the Little Ice Age recorded in the Guliya Ice Core. *Science in China*, 39, 6.
- 1051 Yang, Y., Li, Q., Ai, M., Shi, Z., Yan, J. (1991), Some queries for the Hotan earthquake 1882  
1052 and the Yeeryang earthquake 1889 in Xinjiang. *Northeastern Seismological Research*, 7(1),  
1053 87-93. <https://doi:10.13693/j.cnki.cn21-1573.1991.01.014>.
- 1054 Zechar, J. D., & Frankel, K. L. (2009), Incorporating and reporting uncertainties in fault slip  
1055 rates. *Journal of Geophysical Research*, 114, B12407.  
1056 <https://doi.org/10.1029/2009JB006325>.